# Construction of a Quantum Gas Microscope for Fermionic Atoms

by

Vinay Venkatesh Ramasesh

Submitted to the Department of Electrical Engineering and Computer Science
in partial fulfillment of the requirements for the degree of

Master of Engineering in Electrical Engineering and Computer Science

at the

MASSACHUSETTS INSTITUTE OF TECHNOLOGY

September 2013

ARCHIVES
MASSACHUSETTS INSTITUTE OF TECHNOLOGY
OCT 29 2013
LIBRARIES

Copyright 2013 Vinay V. Ramasesh. All rights reserved.
The author hereby grants to M.I.T. permission to reproduce and to distribute publicly paper and electronic copies of this thesis document in whole and in part in any medium now known or hereafter created.

Author ..............................................................
Department of Electrical Engineering and Computer Science
Aug 17, 2013

Certified by ..............................................................
Martin W. Zwierlein
Professor of Physics
Thesis Supervisor

Accepted by ..............................................................
Albert R. Meyer
Chairman, Masters of Engineering Thesis Committee

# Construction of a Quantum Gas Microscope for Fermionic Atoms

by

Vinay Venkatesh Ramasesh

Submitted to the Department of Electrical Engineering and Computer Science
on Aug 17, 2013, in partial fulfillment of the
requirements for the degree of
Master of Engineering in Electrical Engineering and Computer Science

## Abstract

This thesis reports the construction of a novel apparatus for experiments with ultracold atoms in optical lattices: the Fermi gas microscope. Improving upon similar designs for bosonic atoms, our Fermi gas microscope has the novel feature of being able to achieve single-site resolved imaging of fermionic atoms in an optical lattice; specifically, we use fermionic potassium-40, sympathetically cooled by bosonic sodium-23. In this thesis, several milestones on the way to achieving single-site resolution are described and documented. First, we have tested and mounted in place the imaging optics necessary for achieving single-site resolution. We set up separate 3D magneto-optical traps for capturing and cooling both $^{23}$Na and $^{40}$K. These species are then trapped simultaneously in a plugged quadrupole magnetic trap and evaporated to degeneracy; we obtain a sodium Bose-Einstein condensate with about a million atoms and a degenerate potassium cloud cooled to colder than 1 $\mu$K. Using magnetic transport over a distance of 1 cm, we move the cold cloud of atoms into place under the high-resolution imaging system and capture it in a hybrid magnetic and optical-dipole trap. Further evaporation in this hybrid trap performed by lowering the optical trap depth, and the cooled atoms are immersed in an optical lattice, the setup and calibration of which is also described here. Finally, we cool the atoms with optical molasses beams while in the lattice, with the imaging optics collecting the fluoresence light for high-resolution imaging. With molasses cooling set up, single-site fluoresence imaging of bosons and fermions in the same experimental apparatus is within reach.

Thesis Supervisor: Martin W. Zwierlein
Title: Professor of Physics

# Acknowledgments

I can't imagine a better way to have spent the past three years than working in the CUA. The atmosphere in our hallway is amazing; the students and postdocs are all enormously talented and moreover, always willing to discuss physics or have ideas be bounced off them. There's a genuine spirit of "we're all in this together" pervading the CUA's multiple labs, an atmosphere that makes it a very difficult place to leave.

I thank Martin Zwierlein for giving me the chance to help build his new lab, Fermi2, and for being a terrific advisor in general. Whenever I got disheartened by the slow progress of our experiment, Martin's optimism would instantly lift my spirits. It's clear that Martin believes completely in his students; this sense surely helped me to keep working hard even when things weren't going well. I also have several fond memories of conversations with Martin over lunch or dinner. He was always happy to give me advice about learning physics or deciding where to go to grad school; he is a mentor in the truest sense of the word. I wish him the best of luck with his future experiments and his new family.

My labmates in Fermi2 deserve profound thanks. This thesis would not be half as long without the efforts of Lawrence Cheuk or Waseem Bakr; how they manage to accomplish so much so fast is beyond me. I thank both of them for teaching me essentially everything I know about atomic physics and for providing an ideal to live up to as a grad student. Congratulations to Waseem on his new job at Princeton, and best of luck! In addition to Waseem and Lawrence, Matt Nichols and Melih Okan were great coworkers. Daily life in Fermi2 was always enjoyable thanks to them. We missed having Thomas Gersdorf and Dave Reens with us this year, a fact which I'm sure caused Nature to breathe a sigh of relief: the thought of Dave, Thomas, and Lawrence working in a lab together must have had the Fermi-Hubbard model cowering in fear. I will miss the whole Fermi2 crew greatly (though I won't miss the gravity jokes so much), and I look forward to seeing excellent results in the future from the machine we all built together.

The rest of Martin's group in Fermi1 and BEC1 were largely responsible for making

life in the CUA fun. I have benefited from their knowledge more times than I can count, especially that of Sebastian Will, Tarik Yefsah, Mark Ku, and the elderly Peter Park. I'm also glad to have known the new additions to our group this year, Wenjie Ji and Jenny Schloss. To Wenjie, thanks for keeping me on my toes during every Zwierlein Group Seminar presentation and for letting me steal your computer every day; I hope Matt and I didn't corrupt you too much. Same goes for Songtai Stephen Li, along with many thanks for livening up our dinner outings with your colorful conversation. Elmer Guardado-Sanchez, the BEC1 undergraduate, was also a great friend; thanks for letting Fermi2 steal you from time to time, and I have every confidence that you will one day learn how to climb a ladder. To both Stephen and Elmer, I hope I was a helpful mentor.

Outside of Martin's group, I would like to thank BEC5 for collectively supporting my optics and electronics thefts. Jesse Amato-Grill taught me almost everything I know about cooking; I enjoyed our Sunday cooking sessions greatly, even though you did most of the work. Ivana Dimitrova taught me the Bulgarian greeting "What're you stealing this time?", while Niklas Jepsen made me understand the true meaning of the Checker Faust. BEC4's Colin Kennedy was, in addition to being a great friend, a great gambling partner; one day I'm sure our bet will be resolved.

All of the professors I've interacted with during my time at MIT have been phenomenal; thanks especially to Wolfgang Ketterle, Nergis Mavalvala, Terry Orlando, Ike Chuang, Barton Zwiebach, Allan Adams, Marc Baldo, Sanjoy Mahajan, and Karl Berggren. Mark Belanger deserves a second round of thanks; like I said in my undergraduate thesis, if any new student in Martin's group is reading this, sign up for the Edgerton shop now! Mark is a wealth of information when it comes to machining.

Finally, the highest thanks to my family, without whom none of this would have been possible. My parents, Ranga and Nalini Ramasesh, and my grandmother, Lakshmi Ramachandran, deserve far more gratitude than I can express here, or in words at all. The care, love, and support they have given me throughout my entire life have had the greatest influence on making me the person I am today. Above all, I hope that I continue to make them proud.

*To my family*

# Contents

1 **Introduction** **19**

1.1 Ultracold Atomic Gases as Tunable Many-Body Systems . . . . . . . 19

1.1.1 Fermions in Optical Lattices—Condensed Matter Simulation . 21

1.1.2 Bosonic Quantum Gas Microscopes . . . . . . . . . . . . . . . 23

1.1.3 Fermi Gas Microscopy . . . . . . . . . . . . . . . . . . . . . . 25

1.1.4 Outline of this Thesis . . . . . . . . . . . . . . . . . . . . . . 26

2 **Theoretical Background** **27**

2.1 Magneto-Optical Trapping . . . . . . . . . . . . . . . . . . . . . . 27

2.2 Quadrupole Magnetic Traps . . . . . . . . . . . . . . . . . . . . . 30

2.3 Evaporative cooling . . . . . . . . . . . . . . . . . . . . . . . . . 34

2.3.1 Dressed State Picture of RF-Evaporation . . . . . . . . . . . . 35

2.4 Optical Dipole Traps and Lattices . . . . . . . . . . . . . . . . . . 36

3 **A degenerate gas of potassium-40 atoms** **41**

3.1 Creating a Sodium BEC . . . . . . . . . . . . . . . . . . . . . . . 41

3.1.1 Sodium Laser System and MOT . . . . . . . . . . . . . . . . . 42

3.2 Sodium Optical Pumping . . . . . . . . . . . . . . . . . . . . . . . 47

3.3 Sodium Magnetic Trapping, Transport, and Evaporation . . . . . . . 49

3.4 Potassium MOT . . . . . . . . . . . . . . . . . . . . . . . . . . . 52

3.5 Sympathetic Cooling . . . . . . . . . . . . . . . . . . . . . . . . . 53

4 **Single-site resolved imaging system** **55**

4.1 Imaging system resolution . . . . . . . . . . . . . . . . . . . . . . . . 55
4.2 Microscope Optics . . . . . . . . . . . . . . . . . . . . . . . . . . . 60
    4.2.1 Experimental Realization . . . . . . . . . . . . . . . . . . . . . 62
4.3 Objective Alignment and Mounting . . . . . . . . . . . . . . . . . . 63

**5 Optical Lattice** **67**

5.1 Overview of the Optical Lattice Setup . . . . . . . . . . . . . . . . . 67
5.2 Lattice Implementation . . . . . . . . . . . . . . . . . . . . . . . . . 69
    5.2.1 Intensity Stabilization . . . . . . . . . . . . . . . . . . . . . . 71
5.3 A Sodium Condensate under the Microscope . . . . . . . . . . . . . . 74
5.4 Lattice Depth Calibration . . . . . . . . . . . . . . . . . . . . . . . . 78

**6 Outlook** **81**

**A Lattice Depth Calculation** **87**

**B MATLAB Code for Calculating Atom Numbers and Phase Space Densities** **91**

# List of Figures

1-1 Post-analysis occupation images obtained with the Harvard bosonic quantum gas microscope, showing clearly the shells present in a Mott insulator. . . . . . . . . . . . . . . . . . . . . . . . . . . . . . . . 24

2-1 (a) Ground and excited states of an atom placed in a 1-dimensional MOT configuration. To the right of the field zero, the detuning of the laser beams from the $|g\rangle \rightarrow |-1\rangle$ transition is lower than that from the $|g\rangle \rightarrow |+1\rangle$ transition. A $\sigma^-$ transition is thus more likely than a $\sigma^+$, pushing the atom back toward the zero. In (b), we show the coils and laser beams for creating a 3D MOT. . . . . . . . . . . . . . . . . . . . 29

2-2 Hyperfine structures of the ground states of (a) sodium and (b) potassium The states are labeled with the $|F, m_F\rangle$ quantum numbers, which are technically only good quantum numbers at low-field. Note that potassium has an inverted hyperfine structure. . . . . . . . . . . . . . . 32

2-3 Potential landscape of a plugged quadrupole trap, schematically depicted in (a). (b) shows the magnetic and optical contributions separately, which add to give the total landscape, shown in (c). Figure concept taken from [34]. . . . . . . . . . . . . . . . . . . . . . . . . . 33

2-4 A schematic representation of the dressed state picture of RF evaporation. In (a), we show the Zeeman effect on two hyperfine states of sodium: the trappable $|F=2, m_F=2\rangle$ state and the untrapped $|F=1, m_F=1\rangle$ state. In the absence of any RF, atoms initially in $|2,2\rangle$ stay in this state (neglecting Majorana flops) and the blue curve forms a potential landscape for the atoms. When RF at frequency $\omega_{RF}$ turned on, but we do not yet take into account the coupling between levels, the eigenstates become as shown in (b): eigenstates have to be labelled not only by their $F$ and $m_F$ values, but also the number of RF photons in the system. At a radius $r_0$, the curves intersect, as the RF was resonant with the Larmor transition at this radius. When we take into account the coupling between states, an avoided crossing opens up at $r_0$, as shown in (c). The lower curve now forms the potential for the atoms, allowing energetic atoms to spill out over the hill and escape the trap. In (d), as the RF frequency is increased, the avoided crossing moves closer to the trap zero, allowing further atoms to escape the trap. 40

3-1 CAD drawing of the main chamber of our experiment's vacuum system. The purple ball represents the 3D-MOT position, loaded by a Zeeman slower for sodium and 2D-MOT for potassium (neither shown in this picture). The blue atoms directly to the left of the MOT represent atoms in the quadrupole trap centered under the microscope. It is in this quadrupole which we achieve sodium BEC and potassium degeneracy. Subsequently, the atoms are transported upwards under the microscope, the subject of later chapters. Figure created by Thomas Gersdorf. . . . . . . . . . . . . . . . . . . . . . . . . . . . . . . . . 42

3-2 Sodium D2 line (589 nm) structure. Frequency separations are taken from [31] . . . . . . . . . . . . . . . . . . . . . . . . . . . . . . . . 43

3-3 Sodium laser system, figure adapted from [?] . . . . . . . . . . . . . . 44

3-4 Beam paths for the sodium and potassium MOT on the experiment table, shown for one arm only. Other arms have essentially the same setup. . . . . . . . . . . . . . . . . . . . . . . . . . . . . . 46

3-5 Sodium Dark SPOT, containing about a billion atoms at $300\mu K$ . . . 47

3-6 Figure repeated from chapter 2, showing the hyperfine states of sodium-23 and potassium-40 in a magnetic field. . . . . . . . . . . . . . . . . 48

3-7 In-situ image of the quadrupole trap with plug, showing the region of low density evacuated by the repulsive plug laser. . . . . . . . . . . 50

3-8 Plot showing the increase in phase-space density at the expense of atom number which occurs during the first stage of our rf-evaporation of sodium. We begin with about 500 million atoms at a phase-space density of about $10^{-5}$, and end the first stage of evaporation with about 120 million atoms at a PSD of about $10^{-2.5}$. . . . . . . . . . . . . . . 51

3-9 Sequence of evaporation leading up to a sodium BEC of $F = 2$ atoms. 52

3-10 Oscilloscope trace showing the signal from a photodiode monitoring the potassium 3D MOT fluoresence. The horizontal spacing on the trace is 1 second, giving a loading time of a little over 2 seconds. . . . 53

4-1 A two-lens imaging system . . . . . . . . . . . . . . . . . . . . . . . . 56

4-2 Plot of the function $J_1(x)/x$, which is the form of an Airy Disk created by an imaging system with finite resolution. . . . . . . . . . . . . . . 59

4-3 An image showing how the placement of a hemisphere enhances the effective numerical aperture of the imaging system. The sine of the maximal angle is increased by the refractive index ratios, thus increasing the numerical aperture by the same factor. See text for details. . 61

4-4 Our realization of the system depicted schematically before. The hemisphere is a combination of a curved surface, the glass comprising the vacuum bucket window, and a super-polished substrate from ATFilms. Figure not to scale. . . . . . . . . . . . . . . . . . . . . . . . . . . . 63

4-5 A schematic of the Fizeau interferometer used to align the microscope objective. . . . . . . . . . . . . . . . . . . . . . . . . . . . . . . 64

4-6 (a) Fringes obtained with the Fizeau interferometry setup without half-blocking the beam, and (b) a proof that these fringes arise from the curved surface by blocking half the beam. . . . . . . . . . . . . . . . 65

4-7 (a) An early design of the microscope mount, showing the plus-sign shape. (b) Note, however, that in the final design, we did not screw the microscop objective into the plus sign, as suggested by this drawing. Figure created by Thomas Gersdorf. . . . . . . . . . . . . . . . . . . 66

5-1 Idealization of the 2d-layer of the optical lattice underneath the microscope. Figure created by Thomas Gersdorf. . . . . . . . . . . . . . . . . 68

5-2 Mounts for the lattice mirrors. (a) Y-axis retroreflection, (b) Y-axis input, (c) X-axis retroreflection, (d) CAD drawing of the X-axis retroreflection. The X-axis input side is not shown as it is not a custom mount. . . . . . . . . . . . . . . . . . . . . . . . . . . . . . . 72

5-3 Schematic of the PI Circuit designed for stabilization. . . . . . . . . . 73

5-4 We used RF tomography to calibrate the TOP trap fields. Sodium atoms in the $|1,-1\rangle$ state (remember that this is the only trappable state in the F=1 manifold) were transferred via an RF pulse into states in the F=2 manifold. The pulse was kept short so that only resonant pulses would transfer atoms; then, the F=2 atoms were imaged. The picture above shows three rings, due to transitions from $|1,-1\rangle$ into $|2,0\rangle$, $|2,1\rangle$, and $|2,2\rangle$. . . . . . . . . . . . . . . . . . . . . . . . . 76

5-5 A sequence of images showing the final states of our movement of the cloud under the surface. The fact that there are two clouds is an artifact of the bounce imaging. . . . . . . . . . . . . . . . . . . . . . . 77

5-6 Pictures of sodium atoms under the microscope, taken (a) along the vertical axis with the microscope objective and (b) via an imaging beam bouncing off of the substrate. The two clouds seen in (b) are an artifact of this bounce imaging: their intersection represents the substrate surface itself. . . . . . . . . . . . . . . . . . . . . . . . . . . 77
5-7 Picture of the atoms held in a hybrid trap with one lattice arm and the magnetic field, viewed along the orthogonal axis with bounce imaging. 77
5-8 A few pictures of a the sodium BEC created under the microscope via evaporation. . . . . . . . . . . . . . . . . . . . . . . . . . . . . . . 78
5-9 Kapitza-Dirac calibration of our optical lattice. . . . . . . . . . . . . 80

# List of Tables

A.1 Parameters for calculating dipole potentials . . . . . . . . . . . . . . . 88

# Chapter 1

# Introduction

This thesis presents progress towards the construction of an experiment with ultracold neutral atoms in an optical lattice: the so-called Fermi gas microscope. In this chapter, we aim to introduce the reader to the field of ultracold atoms and thus place the present work in its proper context within the field. As will be described, the truly novel aspect of the quantum gas microscope lies in its measurement capability, specificially the ability to measure occupancies of individual optical lattice sites. We thus spend some time discussing the new experimental possibilities made accessible by this single-site resolution.

## 1.1 Ultracold Atomic Gases as Tunable Many-Body Systems

Our interest in ultracold atomic gases—and in this thesis, particularly ultracold gases of *fermions*—stems largely from the fact that they realize a quantum many-body system which is highly controllable. To make this claim more concrete, note that an atomic gas at temperature $T$ can be described roughly as consisting of several quantum wavepackets, the spatial extent of which is on the order of the thermal de Broglie wavelength,

$$\lambda_{dB} = \frac{\hbar}{\sqrt{2\pi m k_B T}}, \tag{1.1}$$

where $m$ is the atom's mass. At temperatures high enough that the thermal deBroglie wavelength is much smaller than the mean interparticle spacing in the gas, the gas is effectively classical and well-described by Maxwell-Boltzmann statistics. However, when the gas is cooled to temperatures such that $\lambda_{dB}$ starts to be comparable to the interparticle spacing, the classical approximation breaks down. In such cases the quantum statistics of the atomic species manifest. Bosonic atoms are described by a Bose-Einstein distribution and undergo a phase transition known as Bose-Einstein condensation (BEC) at this temperature, called $T_C$. At a similar temperature, the Fermi temperature $T_F$, Fermionic species also lose their resemblance to a Maxwell-Boltzmann gas, instead obeying Fermi-Dirac statistics. In effect, cooling the gas brings out its quantum nature.

A natural question then arises of exacly *how* cold one's gas must be to see effects of quantum statistics. The above criterion comparing the de Broglie wavelength of the particles to their spacing immediately makes it clear that this temperature depends on the density of the gas. To give an idea of the scales involved, the first BEC, produced in 1995 with sodium atoms, saw a $T_C$ of 2.0 $\mu$K at a density of $1.4 \times 10^{14}$ cm$^{-3}$ [7]. The first degenerate Fermi gas, produced in 1999 with around $1.2 \times 10^6$ atoms, exhibited a $T_F$ of 1.0 $\mu$K [8].

So much for realizing a quantum many-body system; let's move on to controllability. Interactions between atoms are most properly described by an attractive induced-dipole potential at large separations and a hard core repulsion for short ones. However, in an *ultracold* gas, where the momenta of the colliding atoms is such that the de Broglie wavelength $\lambda_{dB} = h/p$ is much larger than the range of the interatomic potential, the interactions are captured equally well by the much simpler contact-interaction model [29]:

$$V(r) = \frac{2\pi\hbar^2 a_s}{\mu}\delta(r) \tag{1.2}$$

Here $\mu$ is the reduced mass of the two-atom system. Note that in this approximation, the precise details of the interatomic potential are replaced by a single parameter, $a_s$, known as the s-wave scattering length. The magnitude of $a_s$ indicates the strength of the interaction, while its sign differentiates between attraction (negative) and repulsion (positive). Tuning $a_s$ thus corresponds to controlling the interactions in an atomic gas.

Feshbach resonances allow precisely this tuning capability in ultracold atomic gases [17]. With a Feshbach resonance, one uses an external magnetic field to tune the scattering length. Near a resonance—characterized by field $B_0$ and width $\Delta$—the scattering length at magnetic field $B$ behaves as

$$a_s(B) = a_{\mathrm{BG}} \left(1 - \frac{\Delta}{B - B_0}\right), \tag{1.3}$$

where $a_{\mathrm{BG}}$ is the background scattering length far away from the resonance. Thus Feshbach resonances allow control over both the magnitude and sign of the interactions.

Perhaps the best demonstration that ultracold Fermi gases constitute an ideal experimental system is the variety of phenomena which has been explored with them. Following their observation and the advent of Feshbach resonances in Fermi gases in 2002, ultracold fermions were used to create molecular BECs and study the crossover from molecular BECs to a Bardeen-Cooper-Schrieffer superfluid, culminating in 2005 with the demonstration of vortices in an ultracold Fermi gas, a signature of superfluidity. More recent developments include the exploration of spin transport, experimental determination of a universal equation of state for fermions at unitarity, and creation of spin-orbit coupled systems expected to display topological order. For this thesis, however, the most relevant experiments on Fermi gases are those conducted in optical lattices, the subject we turn to next.

### 1.1.1 Fermions in Optical Lattices—Condensed Matter Simulation

Optical lattices provide a direct connection between ultracold quantum gases and electrons in solids. Atoms in optical lattices feel a periodic potential due to the optical standing wave; in solids, the periodic potential arises from the ions. The central solid-state concept of electronic band structure is thus equally applicable to atoms in an optical lattice. Indeed, a direct observation of the band structure of an optical lattice was achieved with ultracold fermions in 2005 [19].

However, tunability of interactions via Feshbach resonances allows one to go beyond the non-interacting case. With BECs of repulsive atoms, for example, experiments have explored the nature of the many-body ground state across varying lattice depths, revealing a quantum phase transition between a superfluid and Mott insulating[1] phase [11]. More recently this phase diagram has also been explored in fermionic atoms with both attractive [6] and repulsive [14] interactions.

Stimulating the ultracold atoms community's interest in optical lattices with fermions is the fact that these systems are a near-perfect realization of the Fermi-Hubbard model [9]. This model assumes a single band, contact interactions between particles, and nearest-neighbor tunneling. Despite its simplicity, calculation of its ground-state properties has eluded physicists in all but a few special cases. Thus, experimentally determining the Fermi-Hubbard ground state for given parameters would represent the solution of a long-standing open theoretical problem by experimental means.

Fermi-Hubbard physics is particularly interesting given that it *might contain the minimal ingredients for high-temperature superconductivity.* Unlike conventional superconductors, which are well described by the BCS theory, high-temperature superconductors—such as the cuprates—are not, at this time, understood theoretically. Were such a theory known, one might be able to design materials which exhibit superconducting behavior even up to room temperature. Such considerations make solving the Fermi-Hubbard model an extremely technologically relevant problem.

One of the reasons that the Fermi-Hubbard model is expected to give rise to high-temperature superfluidity lies in the nature of its ground state at half-filling: this is one of the "special cases" described above, where it is known that the ground state is a Mott insulator with antiferromagnetic ordering. Essentially, this is a checkerboard pattern of alternating "spin-up" and "spin-down" particles. Turning to condensed matter, high-temperature superconductivity is seen in materials which, when undoped, are also Mott insulators with antiferromagnetic ordering. This seemingly suggestive fact might imply that the ground state of the Fermi-Hubbard model at higher fillings exhibits high-temperature superconductivity. It is thus no surprise that simulating the Fermi-Hubbard model is a such an active area of current research. To date, no group has seen an antiferromagnet in an ultracold Fermi gas; its observation would represent a major stepping-stone on the route to simulating high-temperature superconductivity.

---

[1] A Mott insulator is a material which, under ordinary band structure considerations, would be a conductor; i.e., the highest band is not fully occupied. However, due to repulsive interactions, atoms are localized to individual lattice sites.

### 1.1.2 Bosonic Quantum Gas Microscopes

Prior to the advent of quantum gas microscopy, the standard methods of obtaining data on an atomic cloud were phase-contrast and absorption imaging. In absorption imaging, resonant light is impinged on the cloud and absorbed by atoms, creating a "shadow picture." Phase-contrast imaging uses a far-detuned beam which is not absorbed by the atoms but elastically scattered, with a phase shift indicative of the atomic density [15]. By interfering scattered and unscattered light, one is able to reconstruct an image of the phase shift imparted to the imaging beam by the atomic cloud. While both of these methods have their advantages—phase-contrast imaging uses a more involved setup than absorption imaging, but is nondestructive and can resolve regions of high density that would be "blacked out" on an absorption image—both can be used to detect one of three things: (a) the in-situ density of the atomic cloud within the trap; (b) the momentum distribution of the cloud obtained after a so-called time of flight; and (c) the quasimomentum distribution in a lattice.

As impressive as the results obtained with these imaging methods are, they both suffer from a shortcoming, namely that they are both bulk techniques. As yet, neither has been realized in an imaging system sufficient to resolve individual lattice sites in an optical lattice. That such a system might be useful is easily seen from the discussion of the phases of the Fermi-Hubbard model above; the distinguishing features of the

Mott insulating and antiferromagnetic phases are intimately tied to occupancies of individual lattice sites. Single-site resolution would be invaluable to detecting an antiferromagnet, which, as already mentioned, is a major goal of the ultracold atom community at the current time.[2]

Single-site resolution, or "quantum gas microscopy" as we will call it, was achieved for *bosonic* atoms in optical lattices in 2009 at Harvard University [3] and in 2010 in Munich [4]. Rather than using absorption or phase-contrast imaging, the microscopes used fluoresence imaging, in which light scattered by the atoms was collected to form the image. The distinctive feature of fluoresence imaging which allowed this to work was that one can use fluoresence imaging while simultaneously cooling the atomic sample, and thus pin the atoms in place on a given lattice site while several photons are collected from each atom.

Bosonic quantum gas microscopy allowed for the direct observation of the superfluid to Mott insulator phase transition in the Bose-Hubbard model [2] via images such as those shown in figure 1-1.

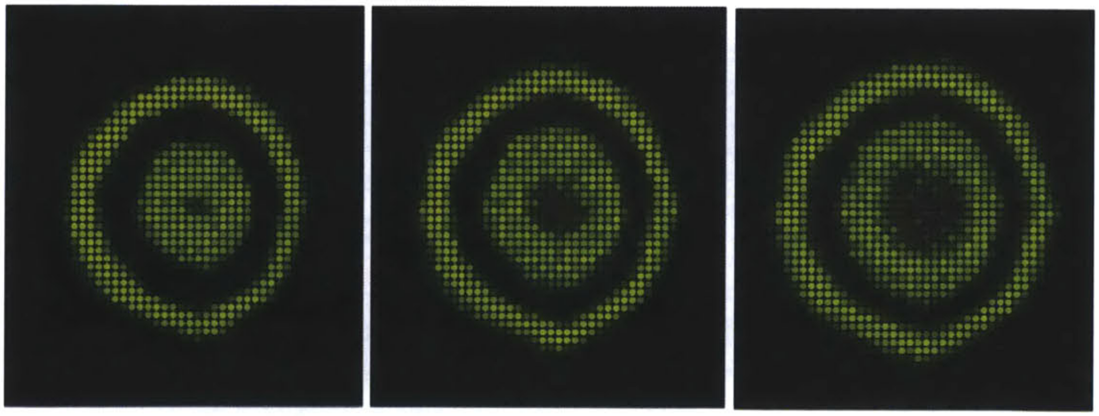

Figure 1-1: Post-analysis occupation images obtained with the Harvard bosonic quantum gas microscope, showing clearly the shells present in a Mott insulator.

---

[2] to be fair, we should note that single-site imaging is not the only conceivable way to detect an antiferromagnet; for example, a Bragg scattering experiment could be performed.

### 1.1.3 Fermi Gas Microscopy

With the success of bosonic quantum gas microscopes, it is natural to apply the same techniques to fermionic species. This thesis reports on the construction of just such an experiment, the "fermionic quantum gas microscope," using fermionic $^{40}$K sympathetically cooled by bosonic $^{23}$Na. One of the most attractive applications of this microscope has already been discussed: exploration of the Fermi-Hubbard model with an eye towards high-temperature superfluidity. However, many other uses exist; we briefly touch on them now.

First, the ability to resolve structures on the length scale of a single lattice site also allows for the creation of optical fields which vary on that same length scale. Using the imaging system designed to achieve single-site resolution in reverse, one can thus project an arbitrary potential in the plane of the atoms. Rather than being restricted to square lattices, lattices of arbitrary geometry, such as triangular or Kagome lattices, can be realized with the quantum gas microscope without any additional beams. This even opens up the possibility of studying, for example, quantum transport along a thin channel connecting two reservoirs at the single lattice-site level.

Quantum gas microscopy also opens up the possibility of new cooling schemes for atoms in optical lattices. One of the groups which achieved bosonic quantum gas microscopy [5] used their system to further cool the gas once in an optical lattice. The technique, known as algorithmic cooling, was demonstrated in an experiment which converted a Mott insulator with four shells into one with only a single shell. Such a novel cooling scheme represents further progress towards the goal of being able to achieve lower entropy samples for use in simulation.

Turning back to many-body physics, one of the recent developments in atomic physics has been the quest to create a system in the lab which features a topologically non-trivial band structure. Apart from a recent experiment in a one-dimensional system [1], as yet, no definitive observation of one of these structures has been made. However, one feature of these systems is that they support so-called edge states, which exist at the boundary of the lattice. With a quantum gas microscope, one might be able to directly observe these edge states as a starting point in investigations of topological materials.

### 1.1.4 Outline of this Thesis

The rest of this thesis is organized as follows.

Chapter 2 presents some relevant theory necessary for understanding the fermionic lattice experiment.

Chapter 3 describes the steps taken to implement sympathetic cooling of potassium-40 via bosonic sodium-23, including the process by which we produce a sodium Bose-Einsten condensate and use sympathetic cooling to obtain a degenerate gas of potassium-40 atoms.

Chapter 4 treats the theory of microscopy and high-resolution imaging before describing the microscope setup in our experiment.

Chapter 5 describes our optical lattice setup, along the way discussing the transport of our cold atomic gas from the initial quadrupole trap up to the substrate where the optical lattice is set up.

Chapter 6 closes with a look at the necessary steps to be taken before single-site imaging of fermions is achieved.

# Chapter 2

# Theoretical Background

This thesis reports the construction of an experiment which cools, traps, and images gaseous clouds of atoms. While the majority of the techniques we use to accomplish these tasks have become standard atomic physics fare in the past several years, we nonetheless present in this chapter a pedagogical introduction to their workings. We first discuss magneto-optical trapping (MOT), the first stage of our experiment. Then, we discuss the quadrupole magnetic trap, which in our experiment follows the MOT stage. Evaporative cooling, a technique we use to cool our atoms once trapped in the quadrupole, is treated next. We conclude by explaining the principle behind the final stage of our experiment, the optical lattice.

## 2.1 Magneto-Optical Trapping

The principle behind magneto-optical trapping has been discussed in great detail in my undergraduate thesis, among other places–see, for example, the original MOT paper by Raab et al. [27]. Here, we present a much more qualitative and abridged discussion. Understanding how a MOT works requires understanding what happens to an atom when it absorbs a photon. This is the so-called dissipative component of the force of light on atoms (the other part of the light force, the conservative part, will play an important role in our discussion of optical lattices later).

The first key point is that when a photon is absorbed by an atom, exciting a transition from, say, state $|g\rangle$ to $|e\rangle$, the atom absorbs the photon's momentum as well as its energy. Second, the probability of an atom absorbing a given photon is maximal when the photons frequency matches the atomic transition frequency (resonance), and is only significant for a small window (the so-called linewidth) of photon frequencies around resonance.

Armed with this fact, we can build up to a MOT, first considering a simpler situation: Doppler cooling. Consider an atom with transition frequency $\omega_0$ subjected to two counterpropagating laser beams, each with the same frequency, $\omega$, such that $\omega < \omega_0$. In this case, a moving atom will, in its rest frame, experience light beams of differing frequencies, due to the Doppler effect. The copropagating beam will be seen to have a lower frequency than in the lab frame, while the counterpropagating beam will have a higher frequency. This brings the counterpropagating beam closer to atomic resonance, meaning that the probability of absorbing a photon from the counterpropagating beam is higher than that for the copropagating beam. The momentum kicks from the counterpropagating beam tend to oppose the velocity of the atom, slowing its velocity.

Doppler cooling schemes localize atoms in momentum space but not in position. To accomplish this, we must add a position-dependent force. In a MOT, this additional confinement comes from a combination of two effects: the beam polarizations and an added magnetic field which varies as $B = Bz$, where $z = 0$ is the trap center. This magnetic field splits the excited state into Zeeman sublevels, say $|-1\rangle$, $|0\rangle$, and $|+1\rangle$. The magnetic field is such that to the right of the origin, the energy of $|+1\rangle$ is higher than that of $|-1\rangle$, while to the left of the origin, the opposite is true. We give the counterpropagating beams opposite circular polarizations such that the beam traveling to the left can only excite a transition to $|-1\rangle$, and the beam traveling to the right can only excite a transition to $|+1\rangle$. So we have realized the exact analogue of Doppler cooling, except in position space: an atom to the right of the origin is more likely to absorb a photon which will push it towards the left, and vice versa. Hence, the atoms will be trapped near the zero of the magnetic field. With six laser beams, one can realize a 3D MOT. Figure 2-1 shows this in detail.

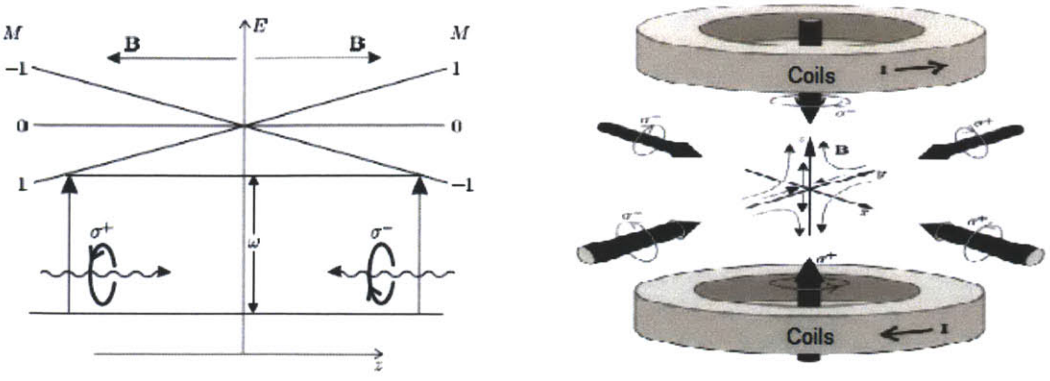

(a) (b)

Figure 2-1: (a) Ground and excited states of an atom placed in a 1-dimensional MOT configuration. To the right of the field zero, the detuning of the laser beams from the $|g\rangle \rightarrow |-1\rangle$ transition is lower than that from the $|g\rangle \rightarrow |+1\rangle$ transition. A $\sigma^-$ transition is thus more likely than a $\sigma^+$, pushing the atom back toward the zero. In (b), we show the coils and laser beams for creating a 3D MOT.

Because of the finite linewidth of the atomic transition, MOTs can only capture atoms over a small range of velocities, roughly given by $\Gamma/k$, where k is the wavevector of the light–this capture velocity is on the order of 10 m/s. Loading techniques are necessary to convert a hot gas of atoms into a colder gas which can be loaded into the MOT. In our experiment we use two different loading techniques. For potassium atoms we use a 2D MOT, a MOT in two dimensions loaded directly from hot background vapor. The atoms travel along the untrapped direction to reach the 3D MOT. For sodium atoms, we use a Zeeman slower, which uses a counterpropagating laser to slow atoms, with magnetic fields to compensate for the changing Doppler shifts of the slowed atoms. As the theory behind a 2D MOT is explained in my undergraduate thesis [28], and the Zeeman slower is discussed in Thomas Gersdorf's diploma thesis [10], neither will be discussed further here.

For a particular atom, the lowest temperature achievable in a MOT is known as the Doppler limit and is given by $\hbar\Gamma/2k_B$ [21]. Here $\Gamma$, the linewidth of the cooling transition, is the only atom-dependent parameter. For the $^{23}$Na D$_2$ transition, the linewidth is $2\pi \times 9.8$ MHz, leading to a Doppler temperature of 235 $\mu$K [31]; for $^{40}$K D$_2$, the linewidth is $2\pi \times 6.0$ MHz, so the Doppler temperature is 145 $\mu$K [32]. These temperatures are not sufficient to achieve degeneracy at the densities achievable with a MOT; in fact, the phase-space density in a MOT is about six orders of magnitude greater than it is at degeneracy [15]. To reach higher phase-space densities, the method we employ is RF-induced evaporation in a magnetic trap, which we now discuss.

## 2.2 Quadrupole Magnetic Traps

Our experiment uses a quadrupole magnetic trap after the MOT stage. Using only magnetic fields, it is possible to create a conservative atom trap for atoms in particular internal states. Known as *trappable* states, these states seek low magnetic fields and are thus trapped at a magnetic field minimum. Different types of magnetic traps exist; one type traps atoms around a magnetic field zero, while others trap atoms at a finite field. Our experiment uses the former type of trap, known as a quadrupole trap. We have, however, built in the capability to run the latter type as well, although as yet we have not needed to use it.

Invented in 1983 by David Pritchard [26] and first observed in 1985 by Migdall et al. to trap sodium atoms [22], magnetic traps are based on two principles:

1. Zeeman effect: The energy of an atom in a given internal state varies with the applied magnetic field magnitude. At low fields,[1] the variation is linear. The sign of the interaction is given by the magnetic moment of the atomic state, and can be either positive or negative: positive magnetic moments imply increasing energies with increasing magnetic field strengths, and vice versa for negative moments.

2. Adiabatic theorem: An atom in a given state, subject to a perturbation, will not change internal states as long as the perturbation occurs over much longer scales than those associated with the energy differences between eigenstates (i.e., the perturbation frequency is much lower than the Larmor frequency).

---

[1] Low compared to hyperfine splitting over magnetic moment

The application of these principles to explain magnetic trapping is straightforward: atoms moving around in a magnetic field while in an internal state with a positive magnetic moment will stay in that state as long as it is protected by a sufficient energy gap. Because these atoms maintain their internal states, the Zeeman shift acts as an effective potential energy landscape. Since positive magnetic moments imply lowest energies at lowest magnetic field, atoms in states with $\mu > 0$ are called low-field seekers and can be trapped at minima of magnetic fields.[2]

Quadrupole magnetic traps typically employ a pair of anti-Helmholtz coils to create a magnetic field which, near its zero, behaves as:

$$B_x = B'x, B_y = B'y, B_z = -2B'z \tag{2.1}$$

Here $B'$ is a constant that characterizes the strength of the field. Note that this trap is not spherically symmetric: because of the Maxwell equation $\nabla \cdot \vec{B} = 0$, the gradient along the z axis is twice that along the horizontal axes. One can immediately see from the above expression that the quadrupole magnetic field has a zero at the origin, making it the trap minimum or center. Near the origin, the strength of the field is given by

$$|\vec{B}| = B'\sqrt{x^2 + y^2 + 4z^2} \tag{2.2}$$

The surfaces of constant magnetic field, which are also the surfaces of constant energy via $E = \mu B$, are ellipsoids. One can also explicitly write out the potential if the magnetic moment is known:

$$V(x, y, z) = \mu B'\sqrt{x^2 + y^2 + 4z^2} \tag{2.3}$$

For the atoms we use, a graph of the Zeeman energies in different hyperfine states is shown in figure 2-2. For sodium, the trappable states are $|1, -1\rangle$, $|2, 2\rangle$, $|2, 1\rangle$, and (weakly) $|2, 0\rangle$. Potassium, as can be seen, can be trapped in several states, among

---

[2] Atoms with negative magnetic moments are known as high-field seekers and are attracted to regions of high magnetic field, but cannot be trapped because it is impossible to create a magnetic field maximum in free space

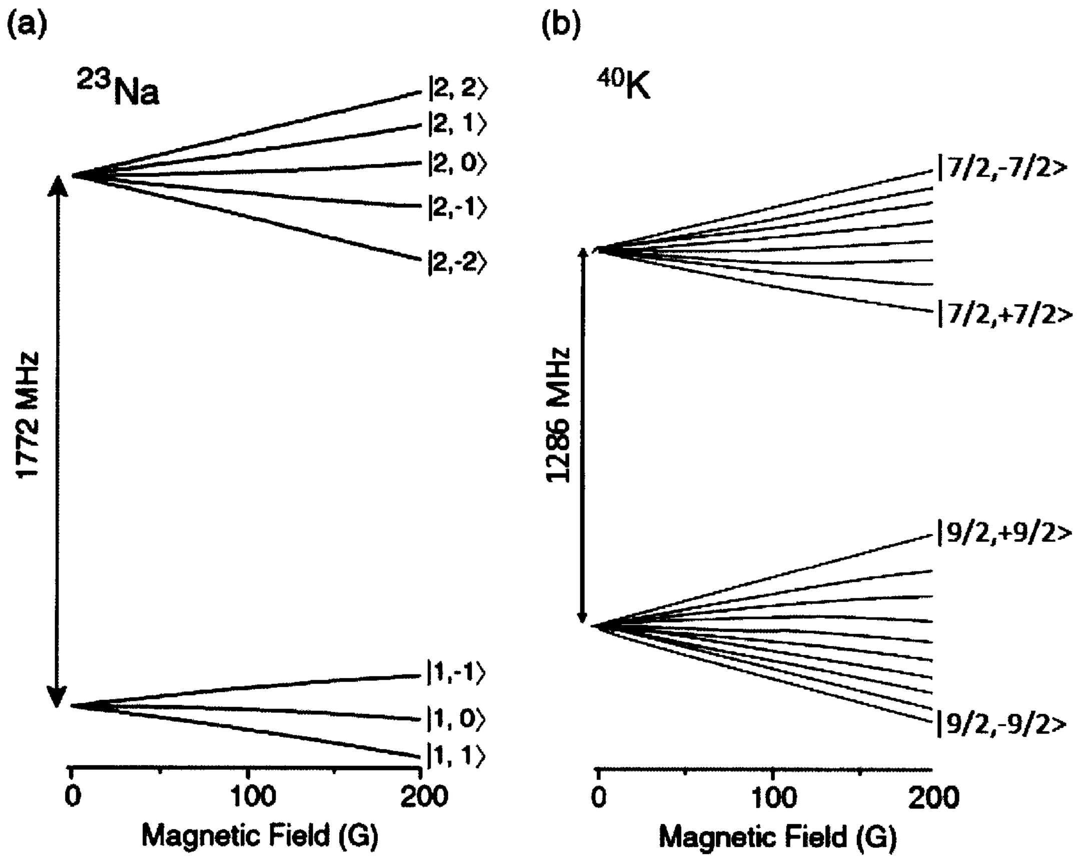
(a)
$^{23}$Na
|2, 2⟩
|2, 1⟩
|2, 0⟩
|2,-1⟩
|2,-2⟩
1772 MHz
|1,-1⟩
|1, 0⟩
|1, 1⟩
0
100
200
Magnetic Field (G)
(b)
$^{40}$K
|7/2,-7/2>
|7/2,+7/2>
1286 MHz
|9/2,+9/2>
|9/2,-9/2>
0
100
200
Magnetic Field (G)

Figure 2-2: Hyperfine structures of the ground states of (a) sodium and (b) potassium The states are labeled with the $|F, m_F\rangle$ quantum numbers, which are technically only good quantum numbers at low-field. Note that potassium has an inverted hyperfine structure.

them $|7/2, -7/2\rangle$ and $|9/2, 9/2\rangle$.

For its simplicity, the quadrupole trap does suffer from a flaw: near the zero of the trap, the energies of all of the internal atomic eigenstates approach the same value. This represents a violation of the adiabatic theorem above, since an atom moving sufficiently fast in a region of low magnetic field would experience a fast perturbation and thus not be constrained to stay in its internal state. Instead, the atom might flip to a high-field seeking state and escape the trap. Such flips are called Majorana flops, and the region in which they are likely to occur is termed the circle of death.

One can quickly derive the extent of the circle of death by comparing the two frequencies involved in the adiabatic theorem: the Larmor frequency, and the frequency associated with a changing magnetic field. When these two become comparable, the adiabatic theorem is violated, enabling Majorana flops. This occurs when $dE/dt \approx E\omega_L = E^2/\hbar$ or–writing $E = \mu B'r$ and noting that $dr/dt = v$, the atomic velocity–when $r^2 = \hbar v/(B'\mu)$. Intuitively, the scalings of the circle of death with atomic velocity and gradient in the above formula makes sense: fast-moving atoms experience a larger perturbation and must go to large radii to achieve large enough energy gaps to stay adiabatic, and atoms in a larger gradient naturally have larger energy gaps and thus have smaller circles of death.

In our experiment, we implement a commonly used solution to the Majorana loss problem known as the optical plug. As we will see in detail in a later section, beams of light blue-detuned from an atomic resonance repel atoms from regions of high intensity.[3]. Thus we plug the Majorana hole by focusing such a blue-detuned laser beam at the center of the trap. A high-intensity focused beam ensures that the trapped atoms do not approach the circle of death and thus maintain adiabaticity. See figure 2-3.

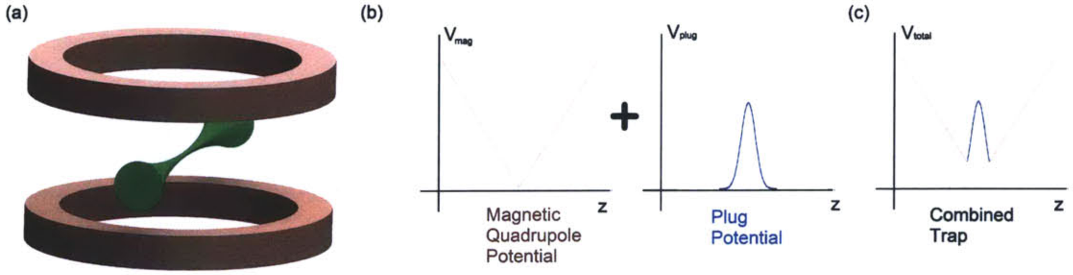

Figure 2-3: Potential landscape of a plugged quadrupole trap, schematically depicted in (a). (b) shows the magnetic and optical contributions separately, which add to give the total landscape, shown in (c). Figure concept taken from [34].

---

[3] We regret that the presentation of ideas in the order we have chosen might confuse the reader. In a previous section, describing MOTs and Zeeman slowers, we discussed the effects of light on atoms in terms of absorption and emission of photons, but now we are talking about light beams repelling and attracting atoms; that is, acting conservatively! It turns out that light acts on atoms both conservatively and dissipatively. We will discuss this properly in a later section, but for now it is enough to note that for light with a frequency near that of an atomic resonance (i.e. MOT and slower light), the dissipative effect dominates, whereas for far-detuned light, the conservative portion of the force dominates. The plug we use is at 532 nm, far-detuned from both resonances of all three of our atomic species (589, 671, and 767 nm)

The conservative nature of the magnetic trap means that by itself it provides no cooling. For cooling, we turn to rf-induced evaporation, or evaporative cooling.

## 2.3 Evaporative cooling

As discussed above, in a MOT one is limited in temperature–by the random nature of Doppler cooling–to several orders of magnitude greater than necessary for degeneracy. Rf-induced evapoartion is a technique which bridges this gap. This technique lowers the temperature of the gas by selectively forcing high-energy atoms to leave the trap and allowing the gas to rethermalize via collisions.

An rf pulse at a frequency $\omega_{RF}$ induces transitions between hyperfine states of an atom if $\omega_{RF}$ matches the frequency of the transition between the two states. Because this frequency depends on the local magnetic field, an rf pulse selectively induces hyperfine transitions in atoms which experience a particular magnetic field. In a magnetic trap, this is equivalent to selecting atoms at a given position and flipping their states.

Atoms in the trap which are at the largest distances from the trap center are the ones with the highest potential energy; in a slight abuse of terminology, these are referred to as the *hot atoms.* To cool the cloud, an rf pulse resonant with the hottest atoms is applied, flipping them into untrapped high-field seeking states. These atoms are expelled from the trap, leaving the cloud in a non-equilibrium velocity/position distribution. Through elastic collisions, this distribution relaxes to a Maxwell-Boltzmann distribution with a slightly lower temperature than before. The rf frequency is continuously lowered to keep expelling the hot atoms, leading to continuously lowering temperatures [16].

Crucial to the success of forced evaporation is the fact that the cloud must rethermalize quickly after high-energy atoms are expelled. If this were not the case, the radiofrequency knife described above would not change the clouds temperature; it would only cut away high-energy atoms. Indeed, in such a case the cloud would not properly have a temperature, since temperature requires equilibration. At the risk of overemphasizing, we state again: simply getting rid of high-energy atoms is NOT the same as cooling! Cooling only occurs when, after the high-energy atoms leave, the rest of the cloud exchanges energy via collisions to achieve an approximately equilibrium distribution of velocities characterized by a lower temperature value than it had before the high-energy atoms were ejected.

The above seemingly minor fact has had immense consequences for the design of our experiment. Remember, our goal is to build an experiment to study degenerate fermions, namely potassium-40 and (later) lithium-6. However, a gas of fermionic atoms all in the same internal state tend to avoid each other. The reason for this is that fermionic atoms in the same internal state ("spin-polarized") cannot undergo s-wave collisions, i.e. collisions in which the relative wavefunction is symmetric. They can only undergo collisions in which the relative wavefunction is antisymmetric, of which the lowest-energy ones have p-wave symmetry. Unfortunately, the temperature at which p-wave collisions are largely suppressed is much higher than degeneracy temperatures[4] . Thus, we added bosonic sodium to our experiment. Sodium and potassium have scattering properties favorable enough to allow the use of sodium as a sympathetic coolant for potassium, which, as later chapters describe, is exactly what we do in our setup.

### 2.3.1 Dressed State Picture of RF-Evaporation

A slightly different picture of rf-induced evaporation is given in terms of dressed states. In the dressed state picture, the effect of turning on a radiofrequency field is considered not simply as inducing spin-flip transitions but rather as an additional term in the Hamiltonian. In this picture it is thus the eigenstates of the Hamiltonian which are modified; rather than the original $|F, m_F\rangle$ eigenstates, with the addition of the rf field the eigenstates get "dressed" by the rf photons to become $|F, m_F; n\rangle$, where

---

[4] Why is this? For a quick estimate, the energy associated with p-wave collisions between atoms a distance $r_0$ apart is $\hbar^2/mr_0$, since the relative angular momentum between the two atoms is $\hbar$. The value of $r_0$ is set by the interaction potential between the two atoms, and is about one to two orders of magnitude larger than the Bohr radius [32]. So p-wave scattering freezes out below several hundred microKelvin.

$n$ refers to the number of rf photons present. However, since an rf photon can induce a transition between $|F, m_F\rangle$ states, the stationary states are actually superpositions of $|F, m_F; n\rangle$ states differing by one in their photon content: $|F, m_F; n\rangle \pm |F', m'_F; n-1\rangle$. As figure 2-4 shows, this leads to the familiar "avoided crossing" effect in quantum mechanics. The adiabatic potential in this case is no longer simply proportional to the magnetic field, but exhibits an avioded crossing where the local magnetic field gives Larmor frequencies resonant with the applied rf.

The essential feature of forced evaporation–expelling high-energy atoms from the trap–is viewed in the dressed state picture as a modification of the potential itself so that atoms at large radii naturally spill out of the trap. See again figure 2-4, which illustrates this "lowering the walls" effect graphically. In this picture, applying rf fields of varying power corresponds to introducing avoided crossing gaps of different heights: the higher the rf power, the larger the energy gap. This in turn controls which atoms actually escape the trap: atoms moving fast through the avoided crossing region will not necessarily follow the adiabatic potential that would let them escape. A larger gap will allow faster atoms to be adiabatic, leading to greater trap loss. For more on the dressed state picture of evaporation, including a more in-depth discussion on the adiabaticity condition, see [16].

## 2.4 Optical Dipole Traps and Lattices

In general, optical fields act on atoms in both dissipative and conservative ways. So far in this chapter we have mainly considered the effect of the dissipative interaction, that is, radiation pressure from photon absorption/emission. This process is at work in Doppler cooling, optical molasses, and MOTs. However, for understanding optical dipole traps and optical lattices, it is the conservative portion of the light force which comes into play. Before understanding in depth how the conservative force arises, we first state the essential result of this section: Inhomogenous beams of light can either trap or repel atoms. Beams which are red-detuned from atomic resonance attract atoms, while blue-detuned beams repel them. This process is conservative; it does not change the energy of the atom.

The essence of this result can be understood independently of a particular model for the atom, classical or quantum. An atom in a light beam of frequency $\omega$ takes on a dipole moment proportional to the electric field: $\vec{d}(\omega) = \alpha(\omega)\vec{E}(\omega)$. The frequency-dependent constant of proportionality is known as the polarizability. We average over the fast oscillations of the electromagnetic wave to get that the energy is proportional to

$$U(\vec{r}) \propto -\langle \vec{d} \cdot \vec{E(\vec{r})} \rangle \tag{2.4}$$

Performing some algebra (and noting that $\alpha(\omega) = \alpha^*(-\omega)$) yields that

$$U(\vec{r}) \propto -\text{Re } \alpha(\omega)|E(\vec{r})^2|, \tag{2.5}$$

arriving at the simple fact that the dipole potential is proportional to the square of the electric field, or the light intensity.

The dipole potential expression is obviously only the conservative part of the story; all of the cooling phenomena we discussed in previous sections were consequences of the dissipative part of the interaction. The relevant parameter of the dissipative interaction is the photon scattering rate, which we calculate by equating the classical expression for the power lost to radiation to the photon scattering rate times the photon energy $\hbar\omega$:

$$\Gamma_{sc} = -\frac{\langle \vec{d} \cdot \vec{E} \rangle}{\hbar\omega} \propto -\text{Im } \alpha(\omega)|E(\vec{r})^2|. \tag{2.6}$$

Optical lattices and dipole traps operate in the frequency regime where photon scattering is of negligible importance compared to the dipole force. To see the emergence of this regime we need an expression for the polarizability versus frequency. The simplest way to arrive at such an expression is to model the atom as a classical, Lorentzian electron-on-a-spring. Fortunately, it turns out that the fully quantum result (in the limit of low saturation) gives the same result, which can be easily derived:

$$\alpha(\omega) = 6\pi\epsilon_0 c^3 \frac{\Gamma/\omega_0^2}{\omega_0^2 - \omega^2 - i(\omega^3/\omega_0^3)\Gamma} \tag{2.7}$$

Here $\omega_0$ is the natural transition frequency of the atom and $\Gamma$ is the natural damping rate of the atom.

Inserting this $\alpha(\omega)$ into the above expressions for potential and scattering rate yield

$$U(\vec{r}) \propto \left(\frac{\Gamma}{\omega_0 - \omega} + \frac{\Gamma}{\omega_0 + \omega}\right) I(\vec{r}) \tag{2.8}$$

$$\Gamma_{sc}(\vec{r}) \propto \left(\frac{\omega}{\omega_0}\right)^3 \left(\frac{\Gamma}{\omega_0 - \omega} + \frac{\Gamma}{\omega_0 + \omega}\right)^2 I(\vec{r}) \tag{2.9}$$

Neglecting the $1/(\omega_0 + \omega)$ terms in the case of large detunings $\Delta = \omega - \omega_0$, we get the simplified formulas

$$U(\vec{r}) \propto \frac{\Gamma}{\Delta} I(\vec{r}) \Gamma_{sc}(\vec{r}) \propto \left(\frac{\Gamma}{\Delta}\right)^2 I(\vec{r}) \tag{2.10}$$

So we see that while both the dipole potential and the scattering rate decrease with detuning, the dipole potential scales as $1/\Delta$ and the scattering rate scales as $1/\Delta^2$. In the case of large detunings, the scattering rate is much less than the frequencies associated with the dipole potential and can be safely ignored. Such is the case for optical lattices and dipole traps used in our experiment, which are operated at 1064 nm.

Another consequence of the above expressions is the way in which the sign of the dipole potential depends on the frequency (wavelength) of the light. If the light is red-detuned, i.e. with a longer wavelength than the atomic transition, the potential will be attractive; if it is blue-detuned, the potential will be repulsive. For example, the plug laser we described earlier to prevent Majorana losses in quadrupole magnetic traps is a blue-detuned (532 nm) laser.

One can now easily see how optical dipole traps (ODTs) and lattices are created. In Gaussian ODT's, a red-detuned Gaussian light beam traps the atoms at the beam waist and center, the point of highest intensity. In an optical lattice, a standing wave of light with alternating intensity maxima and minima gives rise to a periodic potential with a period half the size of the light wavelength. Optical lattices along orthogonal lattices can be combined to give rise to 2-dimensional and 3-dimensional structures. Although several lattice geometries (Kagome, triangular, honeycomb) can be realized, in this thesis we exclusively deal with square lattices.

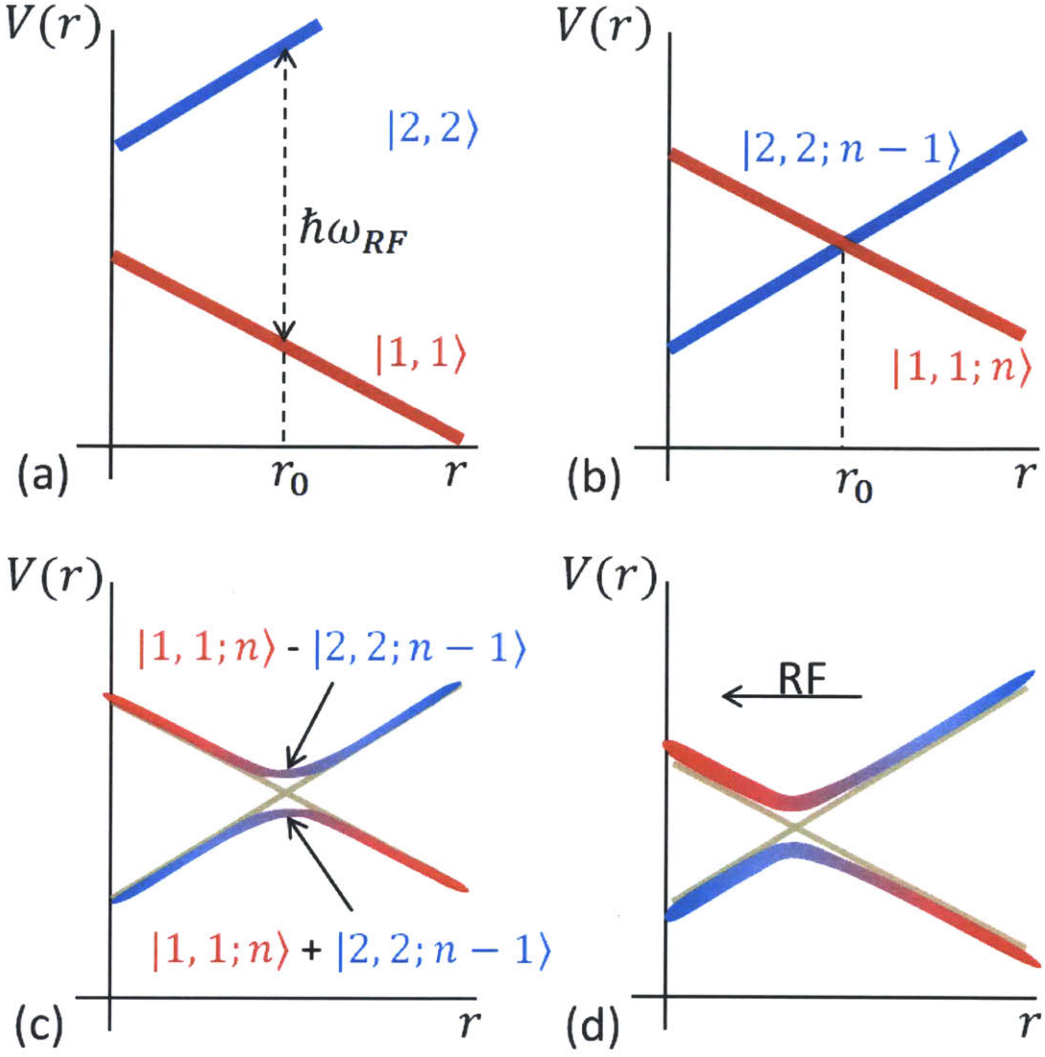

$V(r)$
$|2,2\rangle$
$\hbar\omega_{RF}$
$|1,1\rangle$
(a)
$r_0$
$r$
$V(r)$
$|2,2;n-1\rangle$
$|1,1;n\rangle$
(b)
$r_0$
$r$
$V(r)$
$|1,1;n\rangle - |2,2;n-1\rangle$
$|1,1;n\rangle + |2,2;n-1\rangle$
(c)
$r$
$V(r)$
RF
(d)
$r$

Figure 2-4: A schematic representation of the dressed state picture of RF evaporation. In (a), we show the Zeeman effect on two hyperfine states of sodium: the trappable $|F=2, m_F=2\rangle$ state and the untrapped $|F=1, m_F=1\rangle$ state. In the absence of any RF, atoms initially in $|2,2\rangle$ stay in this state (neglecting Majorana flops) and the blue curve forms a potential landscape for the atoms. When RF at frequency $\omega_{RF}$ turned on, but we do not yet take into account the coupling between levels, the eigenstates become as shown in (b): eigenstates have to be labelled not only by their $F$ and $m_F$ values, but also the number of RF photons in the system. At a radius $r_0$, the curves intersect, as the RF was resonant with the Larmor transition at this radius. When we take into account the coupling between states, an avoided crossing opens up at $r_0$, as shown in (c). The lower curve now forms the potential for the atoms, allowing energetic atoms to spill out over the hill and escape the trap. In (d), as the RF frequency is increased, the avoided crossing moves closer to the trap zero, allowing further atoms to escape the trap.

# Chapter 3

# A degenerate gas of potassium-40 atoms

This chapter describes the process we use to create a cold gas of potassium-40 atoms. An essential step in this process is sympathetic cooling via forced evaporation of sodium-23 in a magnetic trap. This chapter thus begins with a description of our sodium cooling and trapping schemes, culminating in the creation of a Bose-Einstein condensate. After describing our sodium system, we turn to potassium, picking up from the 2D-MOT stage, which was described in my undergraduate thesis [28].

## 3.1 Creating a Sodium BEC

To create a sodium BEC, we begin with a Zeeman-slower loaded MOT. Then, we capture cooled atoms from the MOT in a quadrupole magnetic trap created by the same coils–and thus in the same place–as the MOT. Since this trap is centered on a position 12 mm away from the microscope field of view center, we perform magnetic transport from the original quadrupole trap into another one concentric with the microscope[1]. We plug the Majorana hole in this trap with a 532 nm laser beam and evaporate to get a BEC. In the following sections we expand upon this overview.

---

[1] See figure 3-1 for a picture of our chamber; for a more thorough discussion, the reader is referred to Thomas Gersdorf's diploma thesis [10]

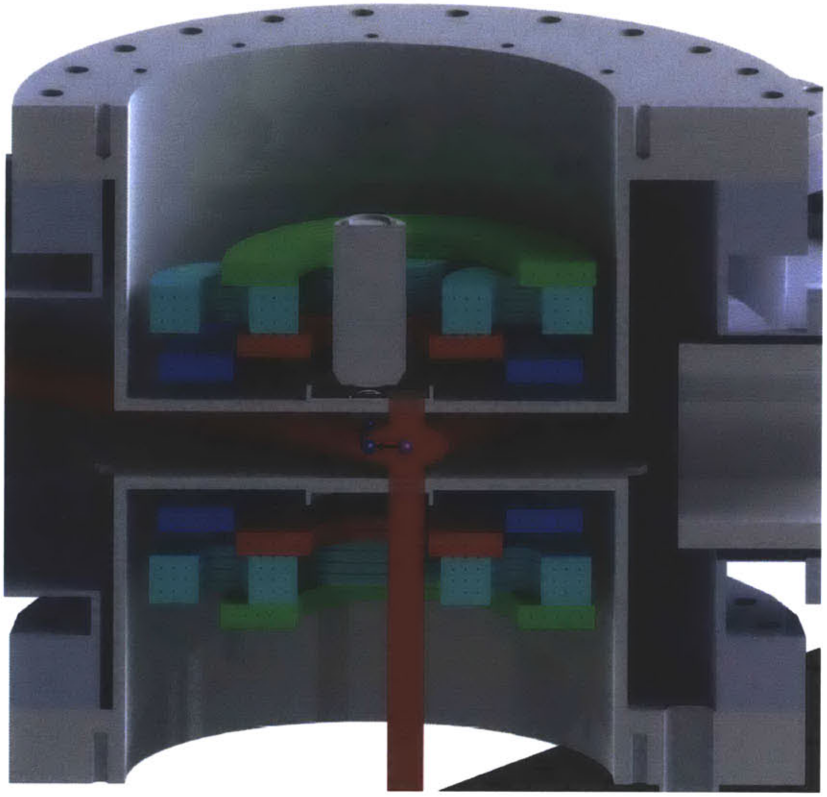

Figure 3-1: CAD drawing of the main chamber of our experiment's vacuum system. The purple ball represents the 3D-MOT position, loaded by a Zeeman slower for sodium and 2D-MOT for potassium (neither shown in this picture). The blue atoms directly to the left of the MOT represent atoms in the quadrupole trap centered under the microscope. It is in this quadrupole which we achieve sodium BEC and potassium degeneracy. Subsequently, the atoms are transported upwards under the microscope, the subject of later chapters. Figure created by Thomas Gersdorf.

### 3.1.1 Sodium Laser System and MOT

The internal structure of the sodium-23 D2 line (589 nm) is shown in figure 3-2. As is standard, we cool and trap with light resonant with the cycling $|F = 2\rangle \rightarrow |F' = 3\rangle$ transition. The possibility of an excitation into a state other than $|F' = 3, m'_F = 3\rangle$ necessitates the use of repumping light on the $|F = 1\rangle \rightarrow |F' = 2\rangle$ transition. For Zeeman slowing, both cooling and repumping frequencies are needed, with both of these red-detuned by 1 GHz to be resonant with hot atoms in the sodium oven. Figure 3-2 indicates all of the frequencies necessary for cooling and trapping sodium.

To generate the above frequencies, we built a laser system based on a solid-state

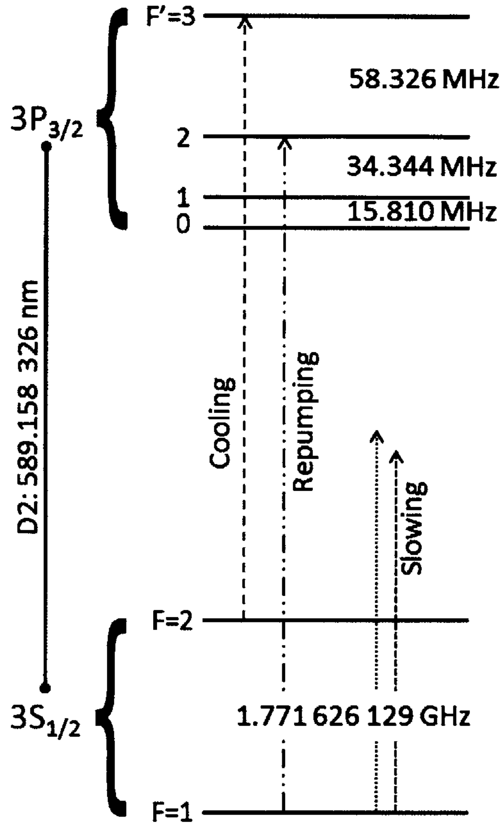
F'=3
2
1
0
58.326 MHz
34.344 MHz
15.810 MHz
3P3/2
D2: 589.158 326 nm
Cooling
Repumping
Slowing
F=2
F=1
3S1/2
1.771 626 129 GHz

Figure 3-2: Sodium D2 line (589 nm) structure. Frequency separations are taken from [31]

589 nm source. This source consists of a Raman fiber amplifier (VRFA-SF from MPB Communications Inc.) operating at 1178 nm, seeded by an 1178 nm grating-stabilized diode laser (Toptica DL Pro) and pumped by an included Ytterbium fiber laser. Following amplification, the 1178 nm light is frequency-doubled in an SHG crystal to yield light at the correct sodium D2 wavelength, 589 nm. We run the laser at an operating power of 1.3 W.

After the SHG crystal, we use acousto-optic modulators (AOMs) and electo-optic modulators (EOMs) to obtain the necessary light frequencies. AOMs shift the frequency of a laser beam via Bragg diffraction off a transverse sound wave, while EOMs use the electo-optic or Pockels effect to add sidebands to a beam[2]. In addition to these tools, we use waveplates and polarization cubes to split light into multiple beams.

---

[2] A treatment of the detailed workings of AOMs and EOMs can be found in almost any thesis in

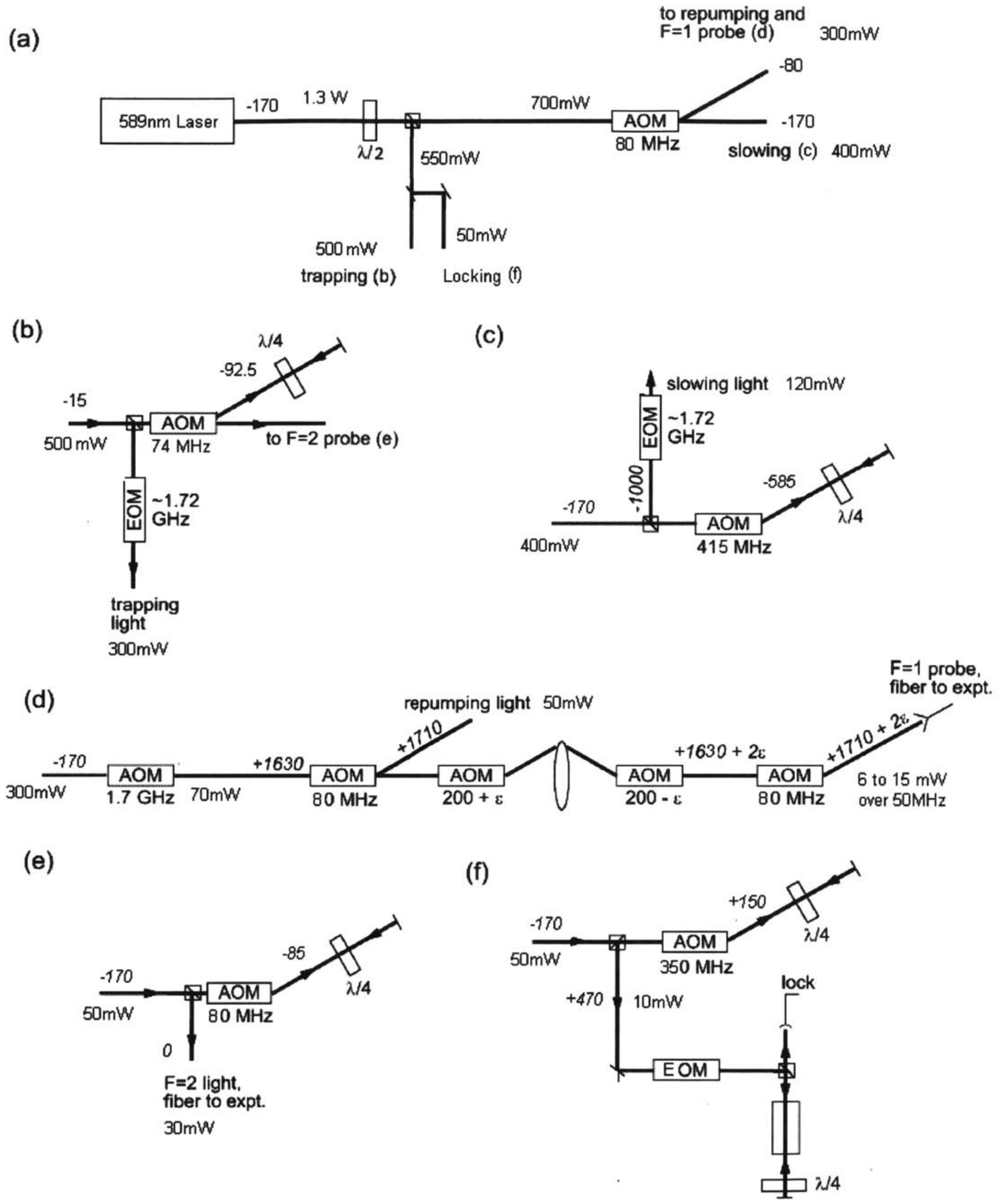
(a)
589nm Laser
-170
1.3 W
λ/2
550mW
700mW
AOM
80 MHz
to repumping and F=1 probe (d)
300mW
-80
-170
slowing (c) 400mW
500 mW
trapping (b)
50mW
Locking (f)
(b)
-15
500 mW
AOM
74 MHz
λ/4
-92.5
to F=2 probe (e)
EOM
~1.72 GHz
trapping light
300mW
(c)
slowing light 120mW
EOM
~1.72 GHz
-1000
-170
400mW
AOM
415 MHz
-585
λ/4
(d)
-170
300mW
AOM
1.7 GHz
70mW
+1630
AOM
80 MHz
repumping light 50mW
+1710
AOM
200 + ε
AOM
200 - ε
+1630 + 2ε
AOM
80 MHz
+1710 + 2ε
F=1 probe, fiber to expt.
6 to 15 mW over 50MHz
(e)
-170
50mW
AOM
80 MHz
-85
λ/4
0
F=2 light, fiber to expt.
30mW
(f)
-170
50mW
AOM
350 MHz
+150
λ/4
+470
10mW
EOM
lock
λ/4

Figure 3-3: Sodium laser system, figure adapted from [?]

Our laser system is shown schematically in figure 3-3. We lock the master laser (Toptica DL Pro) to a frequency such that the SHG output is 170 MHz red-detuned

---

AMO physics, including my undergraduate thesis [28] from the D2 crossover frequency, the average of the $3S_{1/2}\,|F=1\rangle \rightarrow |F'=3\rangle$ and the $3S_{3/2}\,|F=2\rangle \rightarrow |F'=3\rangle$ transition frequencies. This lock is achieved by applying feedback to the grating piezo in the DL Pro, using an error signal generated by four-wave mixing spectroscopy on a sodium vapor cell [23].

With the master laser stabilized, we use AOMs and EOMs to generate the required frequencies of light for magneto-optical trapping, Zeeman slowing, F=1 pumping or repumping ($|F=1\rangle \rightarrow F'=2$), F=2 pumping and imaging ($|F=2\rangle \rightarrow |F'=3\rangle$), and molasses (both $|F=1\rangle \rightarrow F'=2$ and $|F=2\rangle \rightarrow F'=3$)[3]. The beams are coupled into polarization-maintaining fibers (ThorLabs P3-630PM-FC-5) and sent to the experiment table.

Note that the slower beam contains both cooling and repumping frequencies, while for the MOT, separate fibers are used for cooling light and repumping light. This separation is essential, because for sodium we chose to implement a particular MOT variant called the DarkSPOT [18]. In a DarkSPOT, a circular spot (made, in our case, with electrical tape on an optical flat) is placed in the repumper beam path and imaged onto the MOT position, creating a region in the center of the trap where atoms are predominantly in the $|F=1\rangle$ state. In this state, atoms are dark to the MOT light. This has two effects which increase the trapped atom number: it reduces radiation trapping, which contributes an effective repulsive force between the atoms; and it reduces collisions between ground and excited-state atoms which lead to atom loss. As a historical note, when the DarkSPOT was invented in 1992, it allowed for almost an order of magnitude increase in trapped atom density over the original "bright" MOT [18].

The counterpropagating beams required for a MOT are typically produced in one of two ways: separate beam paths or a single retro-reflected beam. In our case, the limitations imposed by our chamber force us to use retroreflection for the bottom beam, but the horizontal beams are separate. We show a schematic representation of one of the MOT beam paths on the experiment table in figure 3-4. After the fiber, the beams are collimated, passed through polarization cubes to produce a defined linear polarization, and then telescoped to a size of ˜3 cm. Finally, the beams pass through a quarter waveplate to become circularly polarized. The powers in each beam are ˜10 mW, as is the dark SPOT repumper.

---

[3] The molasses light is used for fluoresence imaging through the microscope, which will be described in a later chapter.

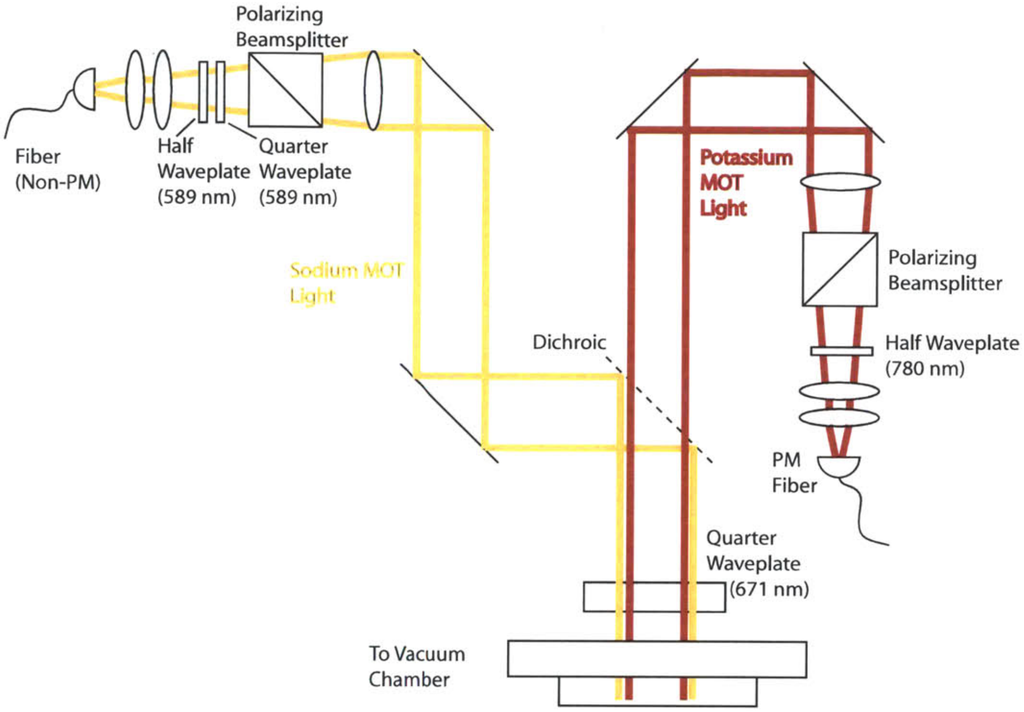
Polarizing
Beamsplitter
Fiber
(Non-PM)
Half
Waveplate
(589 nm)
Quarter
Waveplate
(589 nm)
Sodium MOT
Light
Potassium
MOT
Light
Polarizing
Beamsplitter
Half Waveplate
(780 nm)
Dichroic
PM
Fiber
Quarter
Waveplate
(671 nm)
To Vacuum
Chamber

Figure 3-4: Beam paths for the sodium and potassium MOT on the experiment table, shown for one arm only. Other arms have essentially the same setup.

To generate the magnetic field gradient for the MOT, we pass 37 Amps through the MOT coils in our experiment. These coils were designed to produce a radial gradient of 0.145 G/A/cm and an axial gradient of twice that, 0.290 G/A/cm. Measurements showed that these actual factors are 0.16 G/A/cm (radial) and 0.32 G/A/cm (axial). Thus, 37 Amps corresponds to a gradient of 10.7 G/cm (radial) and 21.4 G/cm (axial).

Figure 3-5 shows a picture of the sodium DarkSPOT in action. After loading the MOT for a total of 4 seconds, the MOT contains on the order of $10^9$ atoms at around $300\mu K$, near the Doppler temperature of sodium, $253\mu K$. Temperatures are determined by time-of-flight imaging: we turn the MOT beams and magnetic fields off, allow the cloud to expand, and take an absorption image. We extract the slope of

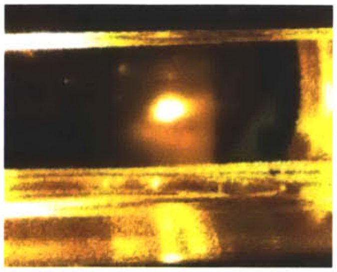

Figure 3-5: Sodium Dark SPOT, containing about a billion atoms at $300\mu K$

the cloud-size versus expansion time curve, yielding an average velocity and thus, a temperature. Note that this method of extracting slopes is necessary for a MOT, but not in the subsequent magnetic traps. There we can simply assume an infinitesimal initial cloud size and extract a velocity from a single time-of-flight shot. In a MOT, however, this overestimates the slope due to the MOT's initial size.

## 3.2 Sodium Optical Pumping

After the MOT, we cool sodium atoms evaporatively in a magnetic trap. As noted in chapter 2, our magnetic trap traps atoms at a field minimum. Thus, to magnetically trap sodium atoms, they must be in a state whose energy increases with increasing magnetic field. Figure 3-6 shows a plot of the energies of the sodium ground state manifold versus magnetic field, the so-called Zeeman shift, repeated from Ch. 2. As the plot shows, the candidates for trappable states are $|2,2\rangle$, $|2,1\rangle$, $|2,0\rangle$, or $|1,-1\rangle$. We rule out $|2,0\rangle$ because it is only weakly trappable at low magnetic fields. Similarly, we rule out $|2,1\rangle$ because hyperfine-changing collisions can turn a pair of $|2,1\rangle$ atoms into one $|2,1\rangle$ and one $|1,1\rangle$ atom, the latter of which can then escape the trap. So only $|2,2\rangle$ and $|1,-1\rangle$ are possibilities for trapping and evaporative cooling.

We need to keep in mind, however, that in this particular experiment we are interested in sodium not only for its own sake, but also for sympathetic cooling of potassium. Looking at figure 3-6 again, the trappable states of potassium are $|9/2,9/2\rangle$ and $|7/2,-7/2\rangle$. Again looking at spin-exchange collisions, we see that we can perform sympathetic cooling either with Na$|1,-1\rangle$ and K$|7/2,-7/2\rangle$ or Na$|2,2\rangle$

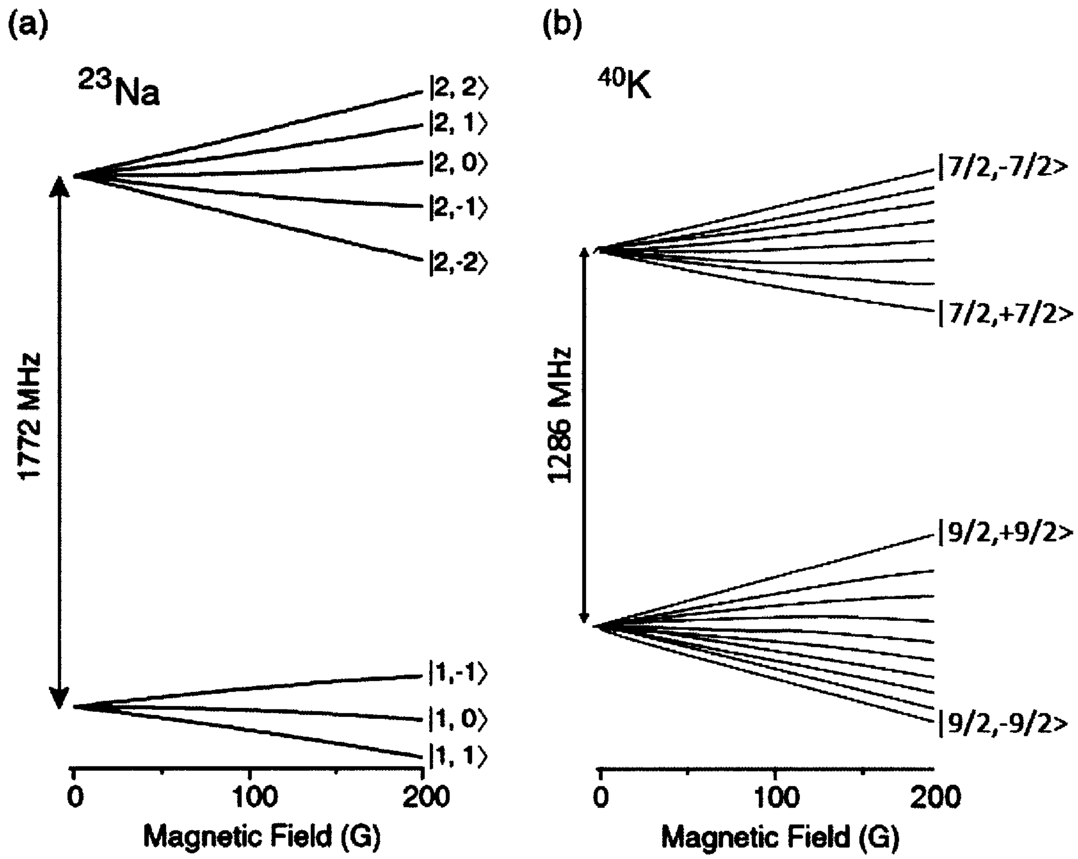
(a)
$^{23}$Na
|2, 2⟩
|2, 1⟩
|2, 0⟩
|2,-1⟩
|2,-2⟩
1772 MHz
|1,-1⟩
|1, 0⟩
|1, 1⟩
0
100
200
Magnetic Field (G)
(b)
$^{40}$K
|7/2,-7/2>
|7/2,+7/2>
1286 MHz
|9/2,+9/2>
|9/2,-9/2>
0
100
200
Magnetic Field (G)

Figure 3-6: Figure repeated from chapter 2, showing the hyperfine states of sodium-23 and potassium-40 in a magnetic field.

and $K|9/2, 9/2\rangle$. We tried both of these approaches, and while we were able to cool sodium to BEC in both the $|1, -1\rangle$ and $|2, 2\rangle$ states, we were never able to successfully magnetically trap potassium in $|7/2, -7/2\rangle$. Possibly this is due to a spin-exchange collision in which $|7/2, -7/2\rangle$ transforms into $|9/2, -9/2\rangle$ and $|9/2, -5/2\rangle$ or $|9/2, -7/2\rangle$ and $|9/2, -7/2\rangle$, possible due to potassium's inverted hyperfine structure. Regardless of the cause, we ended up pursuing the $Na|2, 2\rangle$ and $K|9/2, 9/2\rangle$ cooling strategy, which we will now describe.

In a Dark SPOT, the sodium atoms are predominantly in the $|F = 1\rangle$ state. In between switching off the MOT and switching on the magnetic trap, we thus needed to optically pump the sodium atoms into the $|F = 2, m_F = 2\rangle$ state. We accomplish this with a combination of two optical frequencies. The first is light resonant with the

$|F = 1\rangle \rightarrow |F = 2\rangle$ transition to pump atoms from the $|F = 1\rangle$ to $|F = 2\rangle$ manifold. The second is resonant with $|F = 2\rangle \rightarrow |F = 2\rangle$ and circularly polarized with $\sigma_+$ helicity (we apply a bias field during pumping to have a defined quantization axis). In this way, the $|2, 2\rangle$ state is dark to the pumping light, minimizing cloud heating during pumping. Pumping powers we use are on the order of a milliWatt for both frequencies, and are turned on for a total of 700 $\mu s$.

## 3.3 Sodium Magnetic Trapping, Transport, and Evaporation

With the sodium atoms pumped into the $|2, 2\rangle$ state, we abruptly turn on the MOT coils once again to create a quadrupole magnetic trap. We allow the atoms 100 ms to thermalize, and then perform a "state cleanup" in which we lower the axial gradient to 7.7 G/cm for a total of 300 ms. At this gradient, only the $|2, 2\rangle$ state is supported against gravity; any residual $|2, 1\rangle$, $|2, 0\rangle$ or $|1, -1\rangle$ atoms fall out. After raising the gradient again, we then transport the atoms from the MOT position to their final horizontal position under the microscope, 12 mm away. This is done by by simultaneously ramping down the currents in the MOT coils and ramping up the currents in the coils centered on the microscope position (called "curvature coils" for historical reasons). Over 300 ms, the currents are simultaneously ramped in a cubic spline pattern, chosen so that the slopes of the curves at both endpoints are zero. At the end of this time, the current in the MOT coils is zero. Over the next 300 ms, we ramp up the current in the curvature coils to its final value and allow the atoms another 400 ms to thermalize. With this current, the magtrap gradient is $B'_{axial} = 330$ G/cm ($B'_{radial} = 165$ G/cm). After transport, we have as many as 700 million atoms at a temperature of about 500 $\mu K$. This corresponds to a phase-space density (PSD) of about $10^{-6}$, where phase space density is defined as $n\lambda_{dB}^3$, $n$ being the number density and $\lambda$ the thermal deBroglie wavelength. At the threshold for Bose-Einstein condensation, the PSD is 1, so we are initially six orders of magnitude away.

To plug the Majorana hole in this quadrupole trap, we use a 10 W laser at a wavelength of 532 nm (Spectra-Physics Millenia Pro)[4]. This laser is focused to a waist of 50 $\mu m$ at the center of the quadrupole. The beam path for the plug is exceedingly simple: the output beam from the laser is periscoped onto a breadboard on the experimental table, is passed through a telescope to expand, and then is focused by a lens immediately before it enters the vacuum chamber. This beam path has the drawback that it requires us to shut off the plug with a shutter rather than an AOM, which would be much faster. Unfortunately, this makes thermometry in the quadrupole quite difficult, especially as the cloud gets close to condensation. Initially we had tried to use an AOM; however, thermal lensing distorted the beam shape so drastically that the plug was ineffective. Without the AOM, the beam shape is properly Gaussian, and at 10 W the only lensing symptom we notice is a slight increase in beam waist. In addition, only one element of the beam path is on a movable mount, the mirror we use for everyday alignment. An *in situ* picture of the plugged trap is shown in figure 3-7.

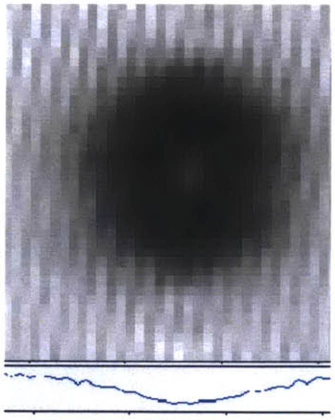

Figure 3-7: In-situ image of the quadrupole trap with plug, showing the region of low density evacuated by the repulsive plug laser.

After the atoms thermalize in the plugged trap, we begin RF evaporation. The applied RF field causes transitions between the $|2,2\rangle$ and untrapped $|1,1\rangle$ state. We evaporate in two stages: first, at the initial gradient, we evaporate for 6s, ramping the

---

[4] Since the atoms spend such a short time in the MOT quadrupole trap, we do not bother to plug it.

RF frequency from 2100 MHz to 1794 MHz with a series of linear stages approximating an exponential curve. To see the efficiency of this evaporation process, we plot a curve of PSD vs. atom number in figure 3-8. We generated this plot with MATLAB using code which is given in Appendix B. The plot (on a log-log scale) is linear, indicating a power-law scaling between the two quantities. We found that the maximum exponent, or log-log slope, we were able to achieve during this stage of evaporation was -2.2. After the first stage of evaporation, we end up with around 120 million atoms at a temperature of 100 $\mu$K, corresponding to a PSD ot $10^{-3}$.

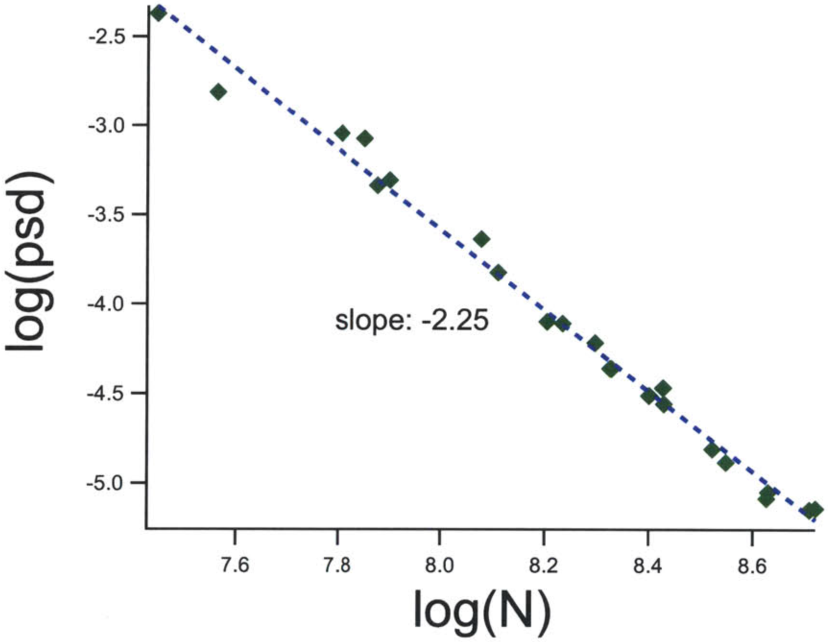

Figure 3-8: Plot showing the increase in phase-space density at the expense of atom number which occurs during the first stage of our rf-evaporation of sodium. We begin with about 500 million atoms at a phase-space density of about $10^{-5}$, and end the first stage of evaporation with about 120 million atoms at a PSD of about $10^{-2.5}$.

At this point in the evaporation, the lifetime of the cloud in the plugged trap is on the order of 10s, indicating three-body losses caused by too high a density of atoms in the trap. To solve this problem, we decompress the trap by a factor of 2/3 over the course of 200 ms (to keep the plug aligned, we use offset fields and vary the current as the decompression progresses). From this point, we continue evaporation, taking 5 seconds to ramp the frequency from 1792 MHz to around 1773 MHz. This yields a

Bose-Einstein condensate, as shown in the sequence of pictures in figure 3-9. Using this method, we have been able to produce BECs with as many as 2 million atoms.

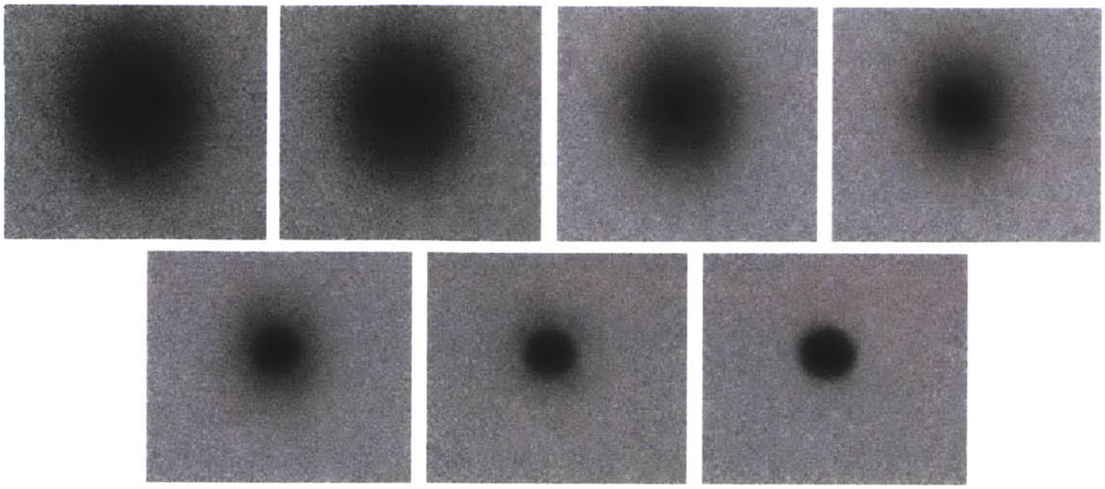

Figure 3-9: Sequence of evaporation leading up to a sodium BEC of $F = 2$ atoms.

## 3.4 Potassium MOT

With a sodium BEC in hand, we now turn to the trapping of potassium atoms. For potassium, we use a bright MOT, which has been used in previous experiments by our group in which sodium-potassium sympathetic cooling was achieved. The first step in this process is building the laser system, which was completed by Thomas Gersdorf and is described in detail in his Diploma Thesis [10]. In brief, a master diode laser (Radiant Dyes Narrowdiode) is stabilized to the potassium D2 crossover frequency; then, light is split off, frequency-shifted with AOMs, and amplified by slave lasers and tapered amplifiers. To carry the light to the experiment table, we use a polarization-maintaining fiber manifold with four inputs and four outputs (although we only use two of the inputs). This allows us to combine MOT and repumper light on the laser table. On the experiment table, the optics are much the same as they are for sodium; the sodium and potassium light is combined using dichroic filters from Semrock.

In contrast to the sodium MOT, the potassium MOT is loaded by a 2D MOT, described in my undergraduate thesis. This 2D MOT performs extremely well compared to traditional Zeeman slowers; we achieve a loading time of about 2 seconds, as shown in figure 3-10.

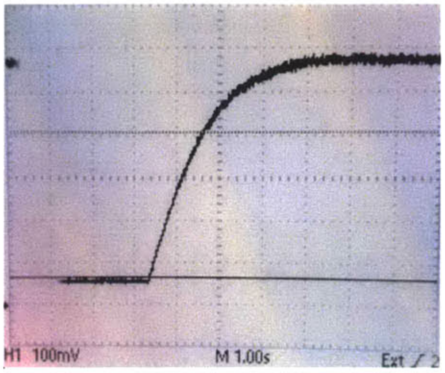

Figure 3-10: Oscilloscope trace showing the signal from a photodiode monitoring the potassium 3D MOT fluoresence. The horizontal spacing on the trace is 1 second, giving a loading time of a little over 2 seconds.

## 3.5 Sympathetic Cooling

While it is possible to capture sodium and potassium together in a dual-species MOT, this suffers from the possibility of light-assisted collisions. Instead, we use a scheme developed earlier by our group [24], which avoids a dual MOT. In this scheme, we first trap sodium in a MOT, pump it into $|2, 2\rangle$, then trap it in the quadrupole and perform state cleanup. Then, we lower the gradient to the initial MOT value, turn on the potassium beams, and load the potassium MOT. In this way, sodium is kept in the magnetic trap while potassium is loaded in the MOT. After K MOT loading, we then pump potassium into $|9/2, 9/2\rangle$ for 500 $\mu s$ and capture both sodium and potassium in the magnetic trap. During this pumping time, the sodium expands freely, but because of the low gradient it was held in, the expansion is small enough that atom losses are negligible.

After sodium and potassium are caught in the MOT quadrupole trap, they are transported to the curvature trap in the same way as described above. We then evaporate, expelling hot sodium atoms. With this evaporation, we find that we are able to get potassium to around 1 $\mu$K. We say "around" because determining the temperature precisely for this cloud is impractical; since we use a plugged trap, accurate fits of the cloud shape to Fermi-Dirac distributions are difficult. Thus, the temperature is determined largely by the temperature of the sodium cloud being used to sympathetically cool the potassium. Assuming these two clouds equilibrate quickly, they should be at roughly the same temperature.

# Chapter 4

# Single-site resolved imaging system

This chapter describes the novel feature of our experiment, the microscope optics capable of resolving fluoresence from single optical lattice sites. High resolution requires a high numerical aperture optical system, a relationship we describe in the first section of this chapter. Like the bosonic quantum gas microscope developed in Markus Greiner's group at Harvard [3], our microscope uses a lens placed extremely close (10 $\mu m$) to the atoms in the optical lattice to achieve high numerical aperture. Unlike the Harvard system, however, all of our optics are placed outside the vacuum chamber. We describe these optics in section 2. In section 3, we discuss the alignment of the microscope objective and its mounting system using Fizeau interfermetry. Finally, the transport of atoms from the curvature trap to their final position under the microscope is discussed.

## 4.1 Imaging system resolution

In general, the resolution of an imaging system is deterined by its numerical aperture, a measure of the amount of light collected by the system. For an imaging system which can collect all of the light rays in a cone of half-angle $\theta$, working in a medium of refractive index $n$, the numerical aperture (NA) is defined as $NA = n \sin\theta$. A system with a given numerical aperture can resolve features with sizes $D$ larger than roughly

$$D = \frac{0.61\lambda}{NA}. \tag{4.1}$$

Here $\lambda$ is the wavelength of the light used for imaging. Because we work in a vacuum chamber, the refractive index for our experiments is $n = 1$. Hereafter we will consider only this case.

It is instructive to derive eq. 4.1 using standard Fourier optics methods. Consider the imaging system shown below, which images plane $O$ onto plane $I$ using lenses which have focal lengths $f_1$ and $f_2$, respectively. To see the effects of finite numerical aperture, we place an artificial aperture in front of the first imaging lens. In real imaging systems, this aperture does not have to be a physical aperture, but can simply represent the finite size of the lens.

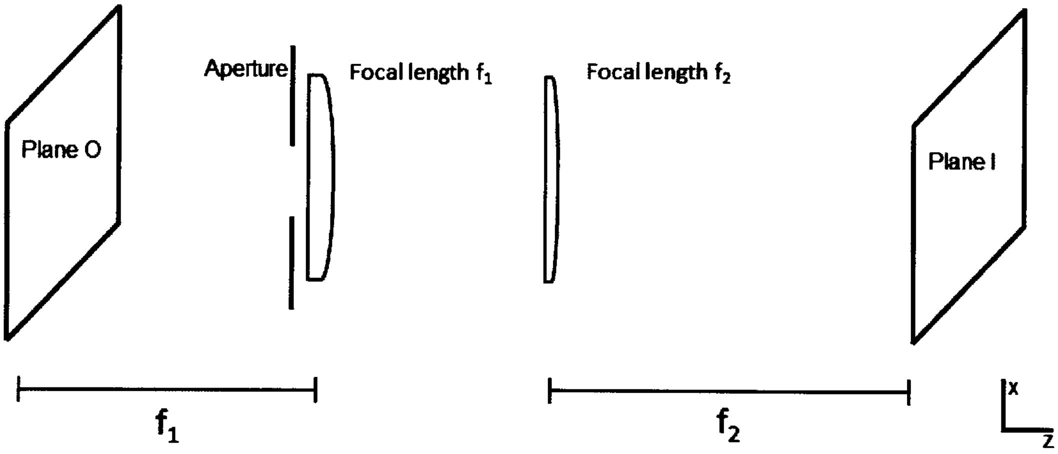

Figure 4-1: A two-lens imaging system

Imagine a point source at the center of plane $O$ which emits a spherical wave of the form $h(x, y, z) \propto \exp(-ikr)/r$. Here the origin coincides with the point source, and $k = 2\pi/\lambda$ is the magnitude of the wavevector of the imaging light. Assuming a paraxial system, with captured rays nearly horizontal, we expand the wavefunction to lowest order in $x$ and $y$, yielding a function proportional to $\exp(-ikz)$, as expected for rays propagating primarily in the z-direction. Typically one drops this factor and instead works with the function $u(x, y, z) = h(x, y, z)/\exp(-ikz)$, which in our case is

$$u(x,y,z) = \frac{\exp\left((-ik/2z)(x^2+y^2)\right)}{z} \tag{4.2}$$

After the aperture, the function is multiplied by a characteristic function $p(x,y)$ to become

$$u_1(x,y,f_1) = p(x,y)\frac{\exp\left((-ik/2f_1)(x^2+y^2)\right)}{f_1} \tag{4.3}$$

The effect of the lens (which we assume to be ideal, i.e. aberration-free) is to multiply the wavefront by $\exp ik/2f_1(x^2+y^2)$, effectively removing the wavefront curvature to produce $u_2(x,y,z)$:

$$u_2(x,y,f_1) = \frac{p(x,y)}{f_1} \tag{4.4}$$

Next, the wave propagates between the two lenses. We could analyze in detail the effect of this propagation; however, we note that as long as the distance between the lenses is smaller than $a^2/\lambda$, where $a$ is a rough measure of the transverse extent of the wavefront, the beam will not diffract much and will have the same functional form when it reaches the second lens. As $a$ is set by the aperture, on the centimeter scale, the length $a^2/\lambda$ will usually be on the scale of 100 meters and can safely be ignored for our optical systems.

After passing through the second lens, then, the wavefront has the form

$$u_3(x,y,z) = \frac{p(x,y)}{f_1}\exp\left((ik/2f_2)(x^2+y^2)\right) \tag{4.5}$$

To arrive at the distribution which is cast on the image plane, we need an equation for the propagation of a wave in free space by a distance $d$. Invoking the Huygens-Fresnel principle, which treats each point on a wavefront as a source of spherical waves, this equation[1] is

---

[1] A more thorough derivation can be found on most books which treat Fourier optics, including a beginning graduate-level text by Haus [13]. In essence, Haus' derivation expresses the input field distribution as a sum of plane waves and then propagates each one through free space by multiplying by a simple exponential factor. At the end, the inverse Fourier transform is taken to arrive back at a position-space representation.

$$u(x,y) = \frac{i}{\lambda d} \exp{(-ikd)} \int\int u_0(x_0,y_0) \exp{((-ik/2z)((x-x_0)^2 + (y-y_0)^2))} dx_0 dy_0 \tag{4.6}$$

Plugging the expression in 4.5 into the above equation, we arrive at

$$u_I(x,y) = \frac{i}{\lambda f_1 f_2} \exp{((\frac{ik}{2f_2})(x^2+y^2))} \int\int p(x_0,y_0) \exp{(\frac{ik}{f_2})((xx_0 + yy_0))}, \tag{4.7}$$

showing that apart from an overall curvature, the impulse response of our imaging system is given by the Fourier transform of the aperture function $p(x,y)$. From this one can immediately see that larger apertures give higher resolutions: the wider p(x,y) is, the narrower will be its Fourier transform. However, to quantitatively arrive at the numerical aperture relation, we take $p(x,y)$ to be a circular aperture with completely absorbing walls, that is, $p(x,y) = 1$ inside the aperture radius $D/2$ and vanishing otherwise. In this case, the Fourier transform is an Airy disk which can be expressed in terms of Bessel functions:

$$u_I(x,y) = u_I(0,0)\frac{2J_1(\pi D\rho/\lambda f_2)}{\pi D\rho/\lambda f_2}, \rho^2 = x^2+y^2 \tag{4.8}$$

This function, plotted in figure 4-2, is peaked at the origin and drops to zero at a radius $\rho_s = 1.22\lambda f_2/D$ [30]. Using the small-angle approximation, $D$ is related to the system's numerical aperture by $D = 2f_1 NA$. So the point source is blurred to a radius of $\rho_s = 0.61\lambda f_2/f_1 NA$. To relate this to the system's resolution, we use a heuristic known as Rayleigh's criterion, which considers two points resolvable if the Airy disk produced by the first is centered on the zero of the Airy disk produced by the second. In our system, this means that the two points are resolvable if their images are more than $\rho_s$ apart from each other. Because the magnification is $f_2/f_1$, the requirement is that points in the object plane are separated by a distance of $0.61\lambda/NA$ or more, which is the relation we had hoped to derive at the beginning of this section[2].

---

[2] Note that we have implicitly assumed spatially incoherent imaging in this section, as we did not worry about interference between Airy disks. In practice, because we use fluoresence imaging, which consists of light spontaneously emitted from atoms, the assumption of incoherent imaging is

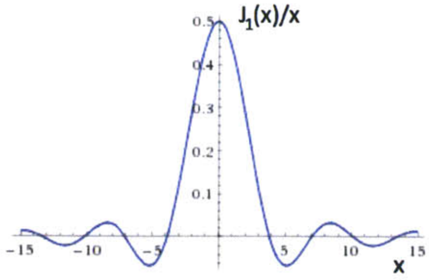

Figure 4-2: Plot of the function $J_1(x)/x$, which is the form of an Airy Disk created by an imaging system with finite resolution.

For fun (and a bit of perspective), let us use the formula we have just derived to calculate the resolution of some of the imaging systems, other than the microscope, which we use in our experiment. These systems are representative of the imaging systems used in current ultracold gas experiments and will serve as a good contrast to the microscope. We have four imaging systems: two for imaging the magnetic trap in which we evaporate (1 cm under the microscope) and two for imaging the cloud after it's moved to the substrate. The magnetic trap imaging paths use a 2-inch diameter, 300 mm focal length lens as the first lens in the imaging system. This corresponds to a numerical aperture of about 0.085, or a resolution of about 4 microns for sodium ($\lambda = 589$ nm) and 5.5 microns for potassium ($\lambda = 767$ nm). For imaging under the substrate, the first lenses are the lattice collimation lenses, which are 200 mm focal-length lenses 1 inch in diameter. Here the numerical aperture is 0.051, meaning the resolution is about 7 microns for sodium and 9 microns for potassium. We should note, however, that because we are not using diffraction-limited optics for these imaging paths, the numbers quoted above are only ideal resolutions, and due to aberrations the actual resolutions of the systems will be poorer[3].

---

justified.

[3] Equivalently, the lenses used in these setups are not ideal, so they do not simply act on the beam by multiplying with the phase factor we used earlier.

## 4.2 Microscope Optics

In this section, we describe our solution for achieving an imaging system that can resolve single lattice sites (on the order of 0.5 micron). This solution is similar, but not identical, to the one used in the Harvard bosonic quantum gas microscope. At the heart of the system is a commercial objective lens from Edmund Optics, the `20X EO M Plan HR Infinity-Corrected Objective`. This lens is a compound lens designed to achieve aberration-free performance when used to image a plane exactly one focal length away (i.e. `Infinity-Corrected`, in the configuration described in the previous section) Keeping the results of the previous section in mind, this lens can be modeled as an ideal thin lens with a focal length of 10 mm combined with an aperture of diameter 11 mm. This leads to the NA value stated on the lens specification sheet, 0.6.

A numerical aperture of 0.6 yields a resolution of essentially $\lambda$, where $\lambda$ is the imaging wavelength. For all three of the species we plan to use in the experiment, this is not quite enough to resolve single sites: sites are separated by 532 nm, whereas the transitions we image on have wavelengths of 589 nm, 767 nm, and 671 nm. To increase the resolution past this threshold, we play the following trick (see figure 4-3): in-between the microscope objective and the atoms, we place a fused silica hemisphere, with the hemisphere centered on the atoms' position. In actuality, of course, the atoms are about 10 microns below the center of the hemisphere, but for an understanding of how the hemisphere enhances numerical aperture, it is helpful to idealize the atoms as lying an infinitesimal distance off-center. Consider, as in figure 4-3(b), the extremal rays from the atoms which is captured by the lens. In the absence of the hemisphere, it is these rays which determine the system's numerical aperture. Adding the hemisphere (figure 4-3(c)) produces no refraction at the curved surface because it's centered on the atoms, but at the flat surface, causes a refraction of the rays according to Snell's law. This is shown more clearly in figure 4-3(d), which makes it clear that the extremal ray in the presence of the hemisphere is at a much larger angle than in its absence. Since the hemisphere increases the sine of the extremal

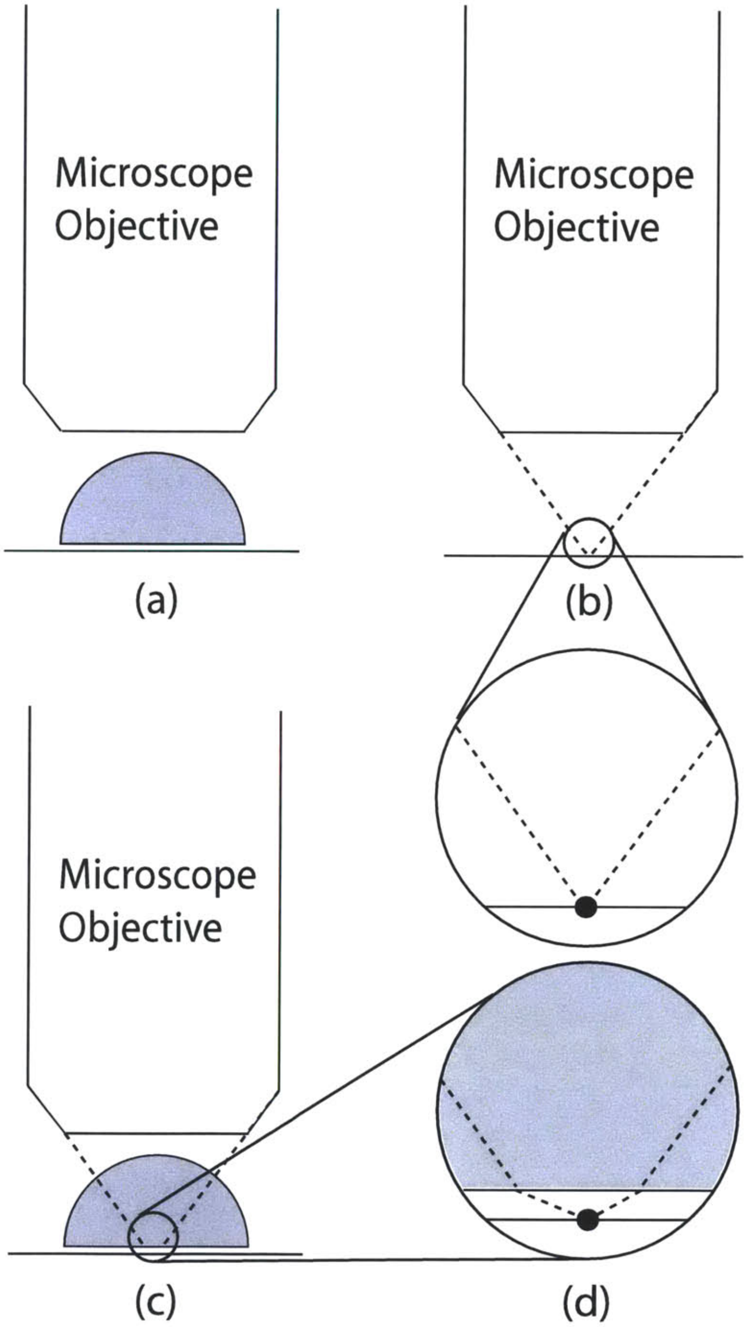
Microscope
Objective
(a)
Microscope
Objective
(b)
Microscope
Objective
(c)
(d)

Figure 4-3: An image showing how the placement of a hemisphere enhances the effective numerical aperture of the imaging system. The sine of the maximal angle is increased by the refractive index ratios, thus increasing the numerical aperture by the same factor. See text for details.

ray's angle by the index of refraction of the fused silica, the numerical aperture is also increased by this factor, $n_{FS} \approx 1.46$. Thus the combined hemisphere-objective system has an ideal NA of 0.876, leading to resolutions of 400 nm (Na), 450 nm (Li), and 525 nm (K).

The argument presented above is admittedly less than rigorous. For example, it does not indicate exactly how far away from the hemisphere the atoms can be for the system to still achieve sufficient resolution. This is an especially important question as atoms trapped close to surfaces might feel unwanted potentials due to this proximity. To answer this question precisely, we use a ray-tracing software (Lambda Research Corporation's OSLO® software). With the results of the simulation, and the experiences of our colleagues who have built quantum gas microscopes [3], we decide to place the atoms $10\mu m$ from the surface of the hemisphere. At this distance, however, we will need to insert a phase correction plate into the imaging path to correct for aberrations [25].

### 4.2.1 Experimental Realization

Our realization of the imaging system described above is shown in figure 4-4. As can be seen, the hemisphere consists of a curved element optically contacted to a vacuum window which features a super-polished substrate on the vacuum side. The atoms to be imaged will be trapped 10 $\mu m$ from the surface of the substrate.

Why a super-polished substrate and optical contacting of the hemisphere? Experimentally, the construction of our imaging system, in addition to the requirements described above, needs to also enable the collection of several photons from each atom. This is necessary to accurately reconstruct each atom's Airy disk; in the face of losses due to inevitable reflections at interfaces, background noise on the camera CCD, the finite quantum efficiency (80%) of our camera, and the small solid angle (about 26% of the full $4\pi$ steradians) of the imaging system, this requirement is all the more stringent. Even ignoring the first two effects, the above two numbers imply that we only capture, at most, 20% of the photons emitted by the fluorescing atoms. For a sense of scale, other quantum gas microscopes collect about a thousand photons per atom

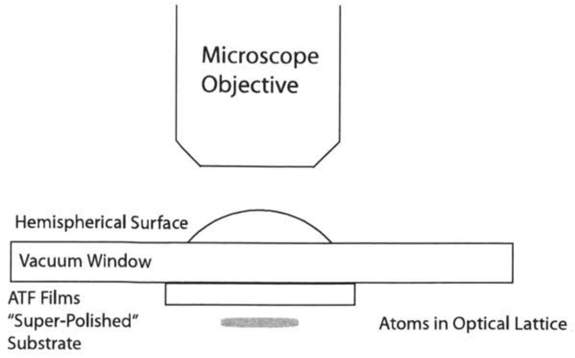

Figure 4-4: Our realization of the system depicted schematically before. The hemisphere is a combination of a curved surface, the glass comprising the vacuum bucket window, and a super-polished substrate from ATFilms. Figure not to scale.

when single-site imaging ([3] and [33]). The upshot of this is that any scattering of imaging light, e.g. that due to Rayleigh scattering via imperfections on a glass surface of standard optical quality, must be minimized. So, we use a super-polished substrate with surface roughness of approximately an Angstrom. Further details of the substrate, as well as information on the optical contacting process, are given in Thomas Gersdorf's diploma thesis [10].

We built a prototype imaging system and tested it in a couple of ways. First, nanospheres of diameter less than 100 nm were imaged to determine the point-spread function of the system, a test which showed that our system was indeed diffraction-limited. Second, Fizeau interferometry was performed to determine the distortion of the wavefront produced by passage through the objective. The distortion we saw was less than $\lambda/4$. For more information on these tests, the reader is again referred to Thomas Gersdorf's diploma thesis [10].

## 4.3 Objective Alignment and Mounting

To align the objective properly with respect to the hemisphere, we used a homemade Fizeau interferometer, schematically illustrated in figure 4-5. In this interferometer, a plane wave created by a reference flat is interfered with the beam created by passing a plane wave through the objective and capturing its reflection (a lens is used to image the objective aperture onto the camera). When the objective is mounted correctly, rays which pass through it (the spherical wave) and hit the hemisphere do so at normal incidence. Upon reflection and a second pass through the objective, they once again form a plane wave, which upon interference with the reference plane wave should reveal straight fringes.

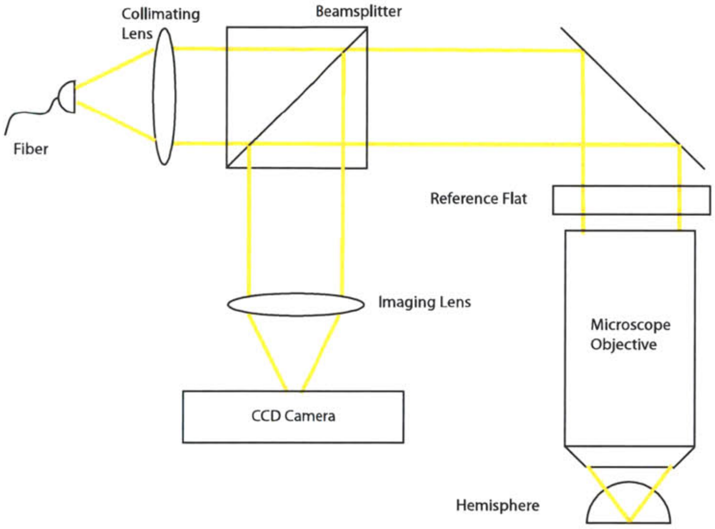

Figure 4-5: A schematic of the Fizeau interferometer used to align the microscope objective.

Pictures of the interference fringes we obtained with the objective placed in the correct position are shown in figure 4-6. To ensure that the horizontal fringes are produced by the reflection off the curved hemisphere surface (and not the flat superpolished substrate) we block half of the beam on top of the objective aperture. Rays which reflect off the curved surface still make it to the camera, as they are incident and reflected on the same side of the beam. Rays which reflect off a flat surface, however, do not make it back, as they are either blocked on incidence or reflection. Since half of the interference fringes survived when we blocked half the beam, the reflection in question was from the curved surface. So, the fringes shown imply a correct alignment of the microscope objective. Once the microscope was aligned in place, a permanent mount was installed. This mount, designed by Matt Nichols, is a stainless steel assembly shaped like a plus-sign, with four holes to mount on the vacuum bucket windows. An early mockup design, not the final one used, is shown in 4-7(a). This initial design called for screwing the microscope objective into the stainless steel directly. In the final design, however, we instead screwed the objective into a ThorLabs CP02 cage plate which was then glued onto metal pieces on the plus sign mount, as shown in 4-7(b).

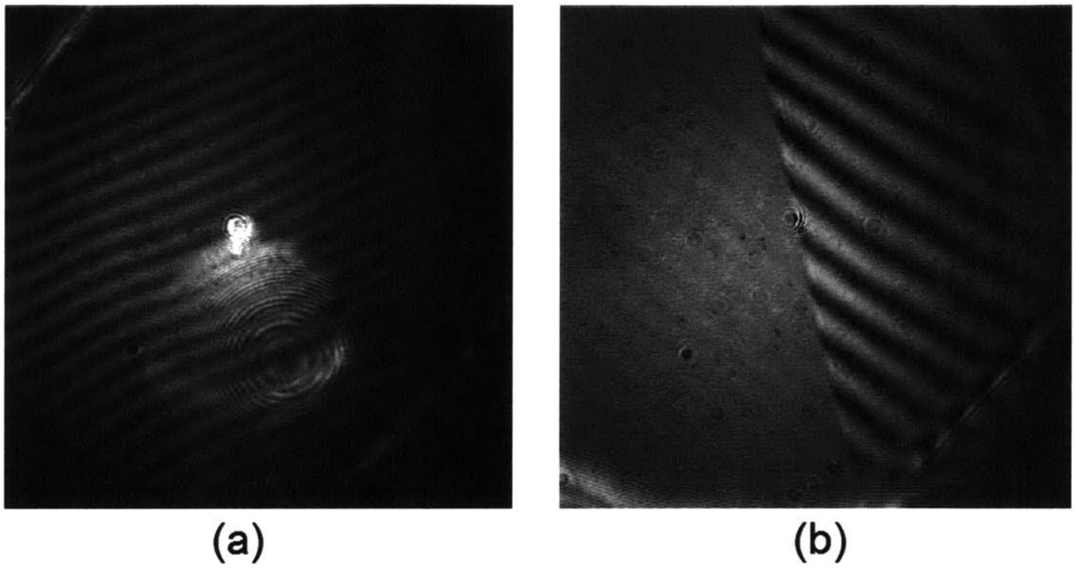

Figure 4-6: (a) Fringes obtained with the Fizeau interferometry setup without half-blocking the beam, and (b) a proof that these fringes arise from the curved surface by blocking half the beam.

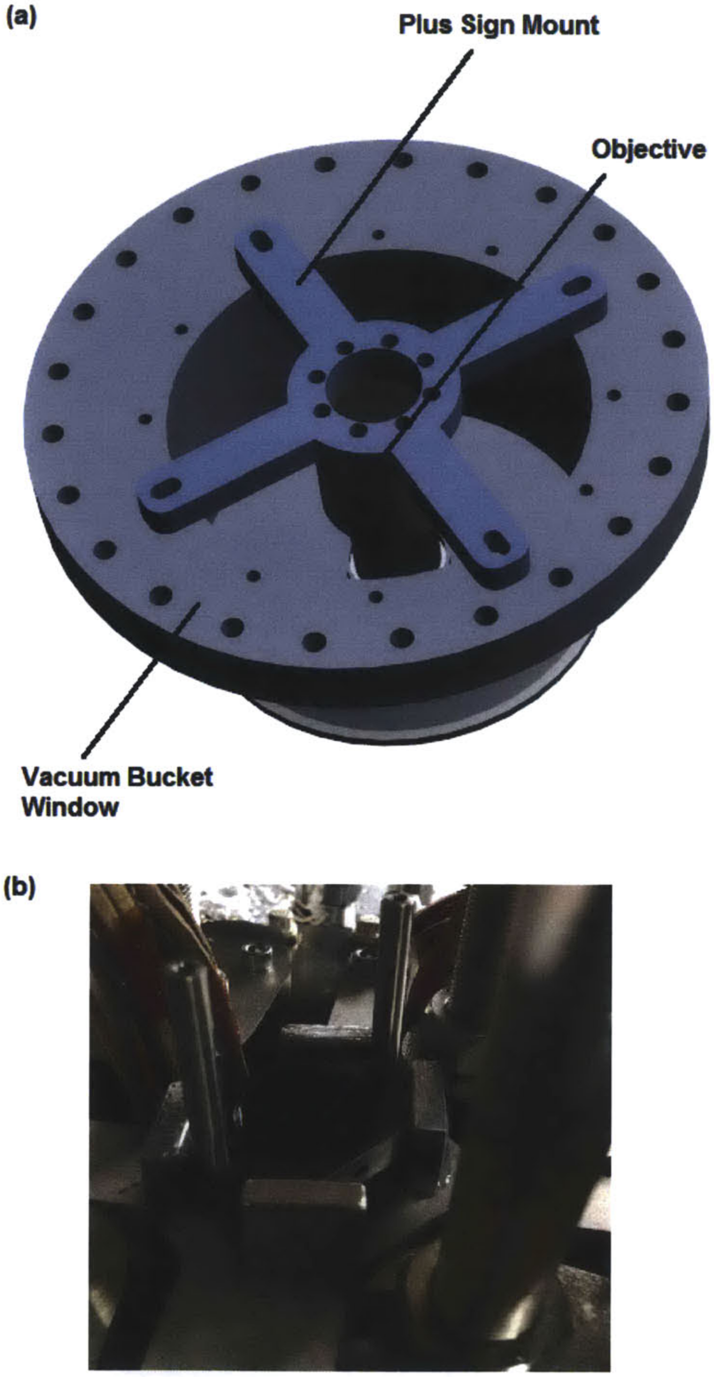
(a)
Plus Sign Mount
Objective
Vacuum Bucket Window
(b)

Figure 4-7: (a) An early design of the microscope mount, showing the plus-sign shape. (b) Note, however, that in the final design, we did not screw the microscop objective into the plus sign, as suggested by this drawing. Figure created by Thomas Gersdorf.

# Chapter 5

# Optical Lattice

This chapter describes the (still in progress) setup and calibration of the optical lattice in which we eventually trap the degenerate potassium atoms. This setup is the heart of our experiment; we aim to study the physics of strongly-interacting fermions in a lattice potential. We give an overview of our setup in section 1. Section 2 describes the optics we use to create the lattice. In section 3, we describe how we transport atoms up to the lattice position and evaporate to BEC, leading into section 4, which closes with a look at the method we used to calibrate the lattice. We emphasize that the lattice setup is still a work in progress, and information contained about the setup in this thesis will likely become outdated very soon!

## 5.1 Overview of the Optical Lattice Setup

Ideally, the goal of our experiment is to create a single 2-dimensional layer of atoms in a planar optical lattice, 10 microns under the super-polished substrate described in the previous chapter. This setup is depicted in figure 5-1. As this setup is created with 1064 nm light, the lattice spacing will be 532 nm.

To create the lattice, we shine in three separate 1064-nm beams, two to create the horizontal square lattice and one for the vertical or z-lattice. The horizontal lattice beams will not be perfectly horizontal, but will bounce off of the substrate at a 10° angle. With this bouncing configuration, the horizontal lattice beams already create

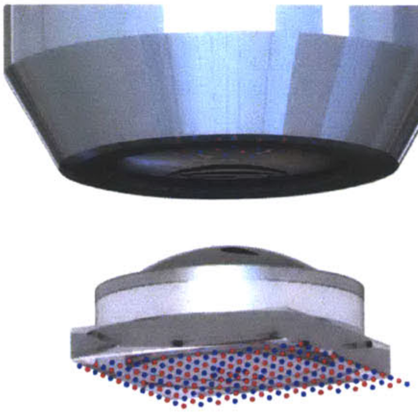

Figure 5-1: Idealization of the 2d-layer of the optical lattice underneath the microscope. Figure created by Thomas Gersdorf.

a vertical lattice with a spacing $\lambda_z$ given by $\lambda/\sin(10°) \approx 3\mu$m. Antinodes (potential minima) of this vertical lattice will exist 1.5, 4.5, 7.5, 10.5 $\mu$m away from the substrate. As discussed, we'd like the atoms to be about 10 $\mu$m from the substrate for imaging, so we use the 10.5 $\mu$m layer. We will develop techniques to load atoms into a single layer of the lattice, or load into multiple layers and then slice away undesired layers.

For initial tests of the imaging system, the vertical lattice created by the two bouncing beams will be sufficient. The third z-lattice beam, to be added later, will create a 532-nm vertical lattice, which, combined with the 3 $\mu$m lattice, will push us further into the 2D regime. Essentially, the creation of a 2D gas requires strong confinement along one direction, effectively freezing the dynamics along that axis. To be a little more precise, a gas is said to be in the two-dimensional regime when all of the relevant energy scales–such as the chemical potential $\mu$ and the temperature $k_BT$–are much lower than the energy scale associated with confinement in the tight direction: $\hbar\omega$. For a deep lattice potential of the form $V_0 \cos(kx)$, a simple Taylor expansion shows that trap frequencies scale as $k\sqrt{V_0}$. Adding the third lattice beam increases both of these values, thus increasing the relevant trap frequency as well. At the time of this writing, only the two horizontal lattice beams have been set up; as noted above, these should be sufficient for single-atom imaging.

We realize this setup with two 1064 nm beams focused to an ellipse with waists of $\sim 25\mu$m and $100\mu$m. This asymmetry is due to the angle of incidence: a circular focus would cause a severely distorted beam on the substrate. With our aspect ratio, the beam hits the substrate in a more circular pattern. In theory, the beams can reach up to 50W power. We can thus calculate the expected value of $V_0$ for both sodium and potassium. This calculation is carried out in Appendix A. The results: for sodium, the lattice depth is about 40 $\mu$K, or 100 times the recoil energy, per Watt of laser power; for potassium, it is about 100 $\mu$K, or about 450 recoils, per Watt.

## 5.2 Lattice Implementation

The coherent laser which forms the basis for our optical lattice is the Mephisto from InnoLight. Light from the Mephisto is split into three beams and coupled into optical fibers which seed Nufern NuAMP Amplifiers. These amplifiers, which require between 50 and 200 mW of seed power, are in theory capable of 50W power output; each one forms one axis of our optical lattice. So far, only two amplifiers have set up. The third will eventually be the vertical lattice, but as described above only two axes are currently functional.

The optics for both the x- and y- horizontal axes are virtually identical after each respective amplifier. Their function, besides the obvious isolation, is essentially threefold:

- Shaping the beam before the final lens which focuses it into the chamber so that the focused beam has the right waists. We use standard Gaussian optics to calculate the pre-lens waists: $w(z) = w_0\sqrt{1 + (z/z_R)^2}$, with $z_R = \pi w_0^2/\lambda$ the Rayleigh range [13]. A spherical telescope followed by a cylindrical telescope accomplishes the beam shaping. In order to avoid thermal lensing, we used very thin fused silica lenses with long focal lengths (see drawing).

- Power control. We use an AOM (IntraAction DTD-274HA6, dissassembled into two separate AOMs) to accomplish power control. As described in a later section, we measure a small amount of the power after the AOM and feedback on the RF power into the AOM to achieve intensity stabilization. The particular AOM we used has an active area on the order of several square millimeters, which we found was necessary to prevent prohibitive thermal lensing. Unfortunately, this has the drawback of reducing the response time of the AOM, which may limit the modulation frequencies we can achieve.

- Frequency shifting. We want to create a potential landscape for our atoms which varies as $V_0(\sin^2(kx) + \sin^2(ky))$. If both x- and y-lattice beams had exactly the same frequency, the potential would be corrupted slightly by an interference term. To see this, note that in the case of same frequencies and identical polarizations, the electric field felt by the atoms would go as

  $$E = \vec{E_0}[\sin(kx - \omega t) + \sin(kx + \omega t) + \sin(ky + \omega t) + \sin(ky - \omega t)] \tag{5.1}$$

  The squared magnitude of this field, whose average determines the intensity, would then have the form

  $$|E|^2 \propto \cos^2(\omega t)[\sin^2(kx) + \sin^2(ky) + 2\sin(kx)\sin(ky)] \tag{5.2}$$

  To avoid the unwanted $\sin(kx)\sin(ky)$ term, we use lattice beams of slightly different frequencies, say $\omega'$ and $\omega$. In this case, the interference term above is multiplied by $\cos(\omega t)\cos(\omega' t)$, which oscillates at the frequency $\omega - \omega'$. In our case, we use the +1st order of the AOM (driven at 40 MHz) for one of the lattice arms and the -1st order for the other, so the oscillation is at 80 MHz, well above trap frequencies and thus negligible[1].

After the beam shaping optics, the beam is sent into the vacuum chamber. On both lattice arms, the large collimated beam is incident on a mirror held by a very stable Polaris mount from ThorLabs. This mirror is the one used for daily alignment, and is placed right before the 250mm lens which focuses the beam into the chamber.

---

[1] This was obvious to all of my labmates, who understood it without going through the math. Since I had to work through it to understand, I included the formulas in this thesis, even though they will likely prove superfluous for most readers.

The final (fixed) mirror mounts in the lattice setup are, for three of the viewports, mounted directly on the vacuum chamber. These mounts were custom-machined to be screwed onto the chamber for added stability. On the retroreflection viewports, the mounts also hold the collimation lenses (250 mm focal length) and retroreflection mirrors. Pictures of the mounts, along with CAD drawings for the retroreflections, are shown in figure 5-2.

It remains to be seen whether mounting the lattice mirrors directly to the chamber is a good idea. With this setup, the position of the lattice is determined by the position of the chamber. The microscope objective, mounted via the plus-sign mount to the top bucket window, is also referenced to the chamber position. Thus, vibrations of the chamber, induced by, e.g., magnetic coil switch-on and switch-off, should not affect the relative position of the lattice and the microscope, as long as these vibrations are common-mode. Certainly for stability, it seems as though the mounts perform their job well; as of a couple weeks into working with the lattice, the retroreflection mirrors have never needed to be realigned after their original alignment (the retroreflection system is an imaging system, so alignment of the retroreflection mirrors is independent of the input beam alignment). Only the input-side mirrors, which are not fixed to the chamber, have needed to be touched on a daily basis.

### 5.2.1 Intensity Stabilization

It is important to stabilize the intensity of the beams used for the optical lattice and, eventually, the dipole trap. Fluctuations in the intensity translate to fluctuations in the potential landscape, which can cause unwanted heating of the atoms in the trap if the fluctuations are at a low enough frequency that the atoms can follow. To actively stabilize our beam power, we measure a small portion of the intensity on a photodiode and feedback on the AOM power.

The system we designed for stabilization is based on one used in the quantum gas microscope at Harvard and documented in the Ph.D. thesis of Amy Peng [25]. One challenge which our particular system must be able to solve is stabilizing the intensity over several orders of magnitude. To do this, we use a logarithmic photodi-

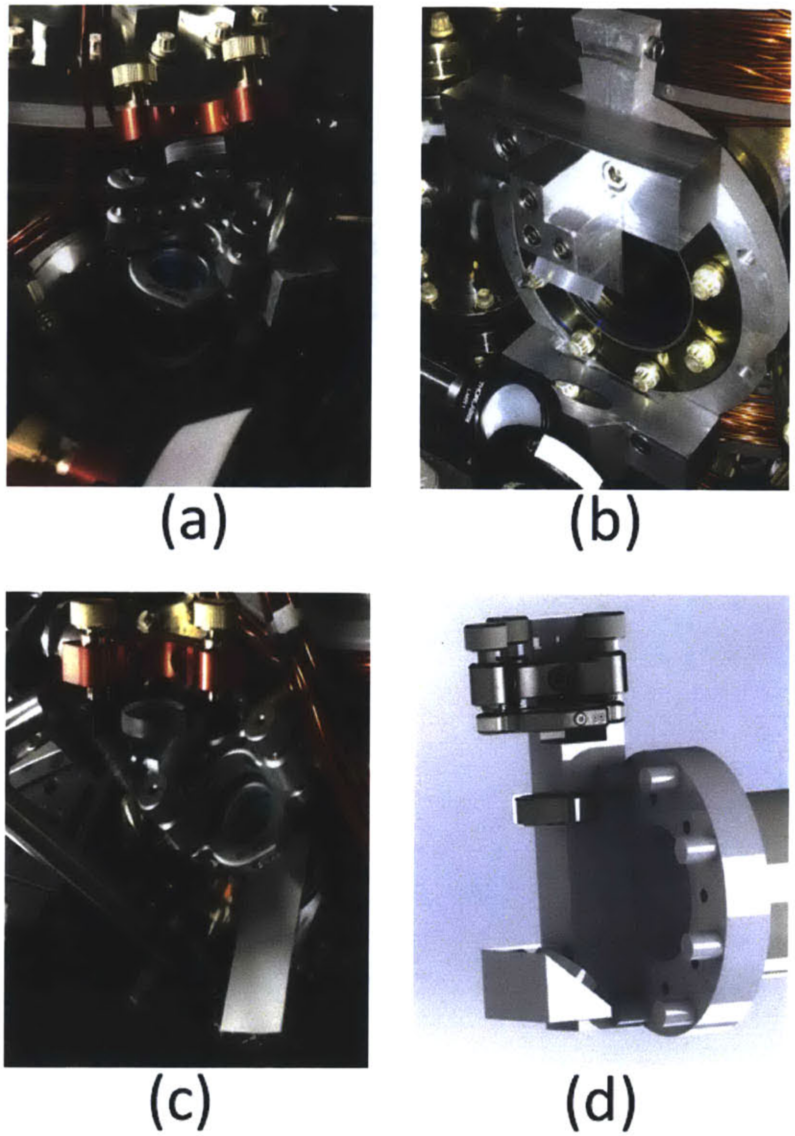

Figure 5-2: Mounts for the lattice mirrors. (a) Y-axis retroreflection, (b) Y-axis input, (c) X-axis retroreflection, (d) CAD drawing of the X-axis retroreflection. The X-axis input side is not shown as it is not a custom mount.

ode; specifically, we connect a standard silicon photodiode (BPX65 from Centronic) to a logarithmic amplifier (AD8304 from Analog Devices, used with the evaluation board). Following advice from the group of Selim Jochim, we cut the cap off of the photodiode to avoid instability due to possible etaloning that occurs when the cap is on. The AD8304 works across a range of 160 dB, or eight orders of magnitude, in photodiode current. It is particularly ideal for this application because it provides an adaptive bias voltage for the for the photodiode, reducing dark current. With the amplifier configured in its default configuration, the buffered output voltage is $V_{LOG} = V_Y \log_{10}(P_{OPT}/P_Z)$, with $V_Y$ at 200 mV/decade and $P_Z$ 110 picoWatts. We feed the output of this voltage to a homebuilt loop filter.

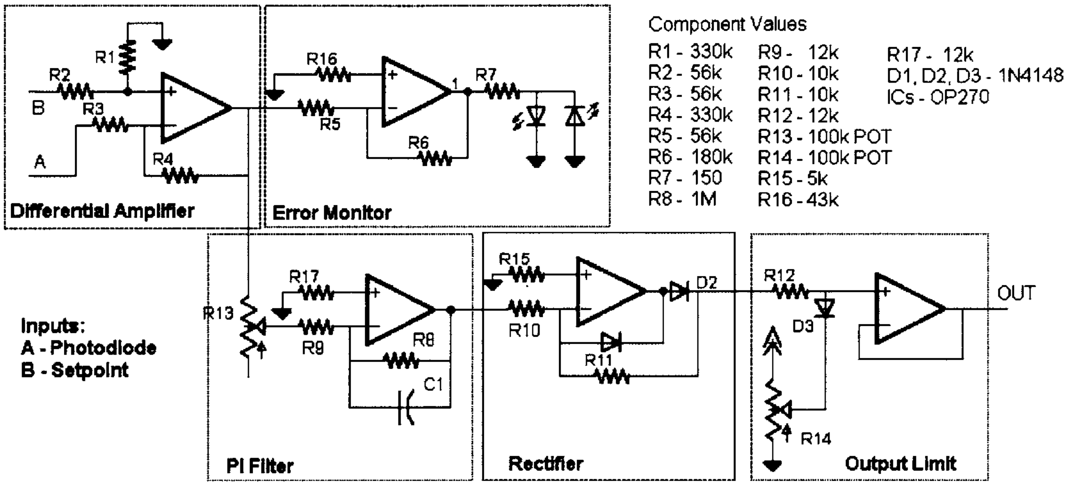
Component Values
R1 - 330k
R2 - 56k
R3 - 56k
R4 - 330k
R5 - 56k
R6 - 180k
R7 - 150
R8 - 1M
R9 - 12k
R10 - 10k
R11 - 10k
R12 - 12k
R13 - 100k POT
R14 - 100k POT
R15 - 5k
R16 - 43k
R17 - 12k
D1, D2, D3 - 1N4148
ICs - OP270
Differential Amplifier
Error Monitor
PI Filter
Rectifier
Output Limit
Inputs:
A - Photodiode
B - Setpoint
R1
R2
R3
R4
A
B
R16
R5
R6
R7
1
R17
R13
R9
R8
C1
R15
R10
R11
D2
R12
D3
R14
OUT

Figure 5-3: Schematic of the PI Circuit designed for stabilization.

The loop filter schematic is shown in figure 5-3. The signal from the logarithmic amplifier and the setpoint from our computer are both fed into a differential amplifier, which outputs a voltage proportional to the difference between those two values. The signal from the differential amplifier is then fed into the loop filter, a standard filter which acts primarily as an integrator but rolls off to a proportional gain at low frequencies. With our element values, the PI corner frequency of the filter is at 200 Hz. The overall gain of this filter is determined by a potentiometer at the input; this is the only controllable value in the circuit. After the loop filter, the signal is rectified and passed into a voltage limiter, the final block of the circuit. These last two blocks are necessary for protecting the exponential amplifier, described in a later paragraph.

The voltage-limiting block of the circuit is based on a passive clamp circuit rather than the active clamp circuit normally used (see, for example, [25]). The reason for this is simple: the low-noise op-amp we have used (OP270) can only tolerate 1.5V between its inverting and non-inverting terminals. In normal applications, this is not a problem, as feedback forces the two terminals to have the same voltage. However, in an active clamp, there is no feedback when the input voltage is below the clamp value, causing a large voltage between the two input terminals. Thus, we use a passive clamp instead; this requires a final buffer to decrease the output impedance.

The output of the PI filter is fed into an exponential amplifier (Analog Devices ADL5330, also with evaluation board). This amplifier controls the RF power arriving at the AOM, which in turn controls the power in the diffracted order, the lattice beam. The ADL5330 can only handle input voltages of up to 1.4V, making the output limit in the PI circuit necessary.

In a test setup, the circuit described above was able to lock to signals of up to 30 kHz in frequency, with the main limit being the AOM rise time (to test this, we moved the beam on the AOM closer to the transducer, and observed an improvement in locking). However, we have yet to test this circuit on the actual lattice setup; since that beam is much larger than the beam we used in our test setup, it is possible that the circuit will not lock at such high frequencies.

## 5.3 A Sodium Condensate under the Microscope

Lattice calibration via the Kapitza-Dirac technique we describe in the next section requires atoms to be trapped in the lattice potential. When last we left our atoms in Ch. 3, though, they were still about a centimeter away from the lattice position.

Several ideas were discussed for moving the atomic cloud up to the final lattice position. The obvious solution was just to move the zero of the magnetic field up to the substrate by adding a vertical offset field. This was initially rejected, however, because while the cloud moved up, there would be no plug, leading to Majorana losses. Instead, we came up with (and tried) several other possibilities:

- One possibility which initially seemed attractive was to use a slightly misaligned 1064 nm beam (which would eventually be the vertical lattice beam) in conjunction with the magnetic gradient as a hybrid trap. Moving the zero of the hybrid trap would bring the atoms up to the substrate. This idea was never tried because we worried that even a shallow z-lattice might inhibit transport.

- Another idea, based on a recent paper from CNRS [20], was to create a 2D gas by combining an RF field with a plugged-trap to create a so-called RF-dressed trap. This idea was particularly attractive because it would already give us a 2D gas which we could then load into one layer of the vertical lattice, eliminating the need for slicing procedures. We spent a few days trying this idea but soon realized that using microwave hyperfine transitions, trappable clouds would have been exceedingly small in size, probably unsuitable for Fermi gases.
- A third idea, which we spent about a week trying to implement, was to use a time-averaged orbiting potential trap, or a TOP trap [15]. In a TOP trap, a rotating bias field is added to a quadrupole trap to move the Majorana-hole faster than the atoms can follow; in effect, it spreads out the Majorana hole into a so-called ring of death. With the TOP trap, the plug would be unnecessary, and since the circle of death is two-dimensional, the cloud could be moved up all the way to the surface without any Majorana losses. Because the high-frequency rotating field necessary in a TOP trap would lead to eddy currents in metallic chambers, TOP traps are usually implemented in chambers with glass walls. Unfortunately, our own chamber was metallic, as when the experiment was first conceived there were no plans to build a TOP. We nevertheless thought to try it, and spent a while setting up additional coils to create the necessary fields. Again, we saw trapping only of tiny clouds. When we measured the fields produced with RF-tomography (see figure 5-4 for details), the reason was apparent: as we suspected, the eddy currents in our chamber greatly reduced the fields inside, making the TOP trap unfeasible.
- Lastly, a Ioffe-Pritchard trap [15] was considered. The coils in our experiment (see [10]) are designed to produce, in addition to a quadrupole magnetic trap, a harmonic Ioffe-Pritchard trap. As this trap has no magnetic field zero, it possesses no Majorana hole and thus would have no need of a plug. Initial

tests of the Ioffe-Pritchard trap in our experiment yielded surprising results; it is possible that an electrical short is present somewhere in the coils. We only made brief attempts at getting this trap to work, however, and it is still possible that it will be used in the future.

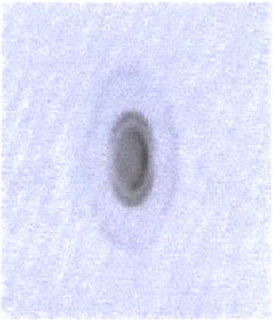

Figure 5-4: We used RF tomography to calibrate the TOP trap fields. Sodium atoms in the $|1,-1\rangle$ state (remember that this is the only trappable state in the F=1 manifold) were transferred via an RF pulse into states in the F=2 manifold. The pulse was kept short so that only resonant pulses would transfer atoms; then, the F=2 atoms were imaged. The picture above shows three rings, due to transitions from $|1,-1\rangle$ into $|2,0\rangle$, $|2,1\rangle$, and $|2,2\rangle$.

After all of these failures, we decided to try the simple, initially rejected, approach of moving the cloud up to the surface simply by shifting the zero of the quadrupole trap. To our surprise, we found that the atoms did not all escape from the trap via Majorana losses; in fact, we could even transport a sodium BEC to the surface and still have atoms (although they were of course no longer in a BEC due to heating). After experimenting with different transport speeds, we settled on a two-stage moving scheme: first, over the course of 50 ms, we move the atoms 98 percent of the way up using a cubic spline ramp; then, over the course of 20 ms, we perform a linear ramp to the final position. We found the two-stage movement necessary to prevent atoms from sloshing up to the substrate and thus being ejected from the trap. It is possible, however, that with current stabilization, this two-stage movement will not be necessary. The movement up to the surface can be seen in figure 5-5. A picture of the cloud from two different axes is shown in figure 5-6. To center the atoms under the substrate, we apply horizontal bias fields.

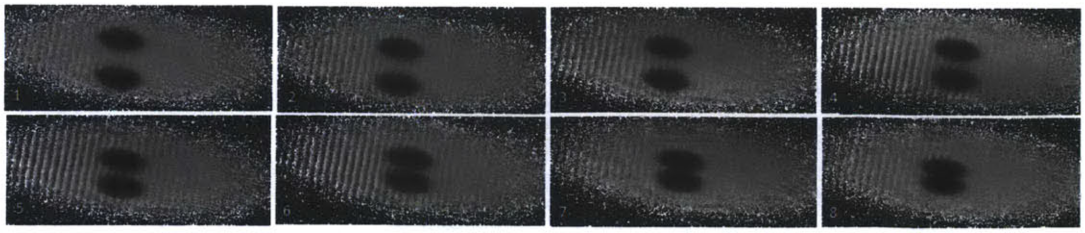

Figure 5-5: A sequence of images showing the final states of our movement of the cloud under the surface. The fact that there are two clouds is an artifact of the bounce imaging.

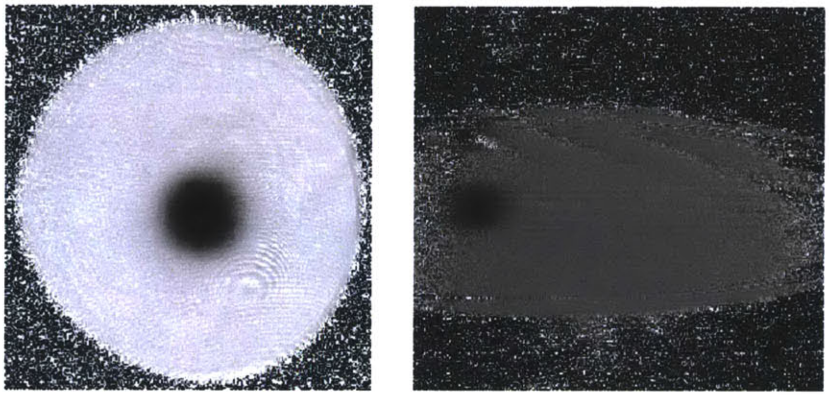

(a) (b)

Figure 5-6: Pictures of sodium atoms under the microscope, taken (a) along the vertical axis with the microscope objective and (b) via an imaging beam bouncing off of the substrate. The two clouds seen in (b) are an artifact of this bounce imaging: their intersection represents the substrate surface itself.

With the atoms in position under the microscope, we turn on the optical lattice beams, allowing the atoms to become trapped by the optical potentials. Then, we move the magnetic zero back down to sit 98% of the way from the initial trap to the substrate. In this way we create a hybrid trap where the radial confinement along the beam is optical and the axial confinement is largely magnetic. Atoms in one axis of the hybrid trap can be seen in figure 5-7.

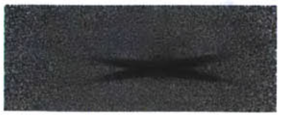

Figure 5-7: Picture of the atoms held in a hybrid trap with one lattice arm and the magnetic field, viewed along the orthogonal axis with bounce imaging.

With the atoms held in the hybrid trap, we perform an evaporation by lowering the beam intensity, allowing the hot atoms to escape. However, we block the retroreflection along one of the lattice axes to promote thermalization (in a truly one-dimensional situation, there is no thermalization). Our evaporation is done over 4 seconds. We use an exponential ramp with time constants of 1 and 1.5 seconds for the x- and y-axes, respectively. After this evaporation, we end up with a BEC in the hybrid trap. Representative pictures of the BEC can be seen in figure 5-8.

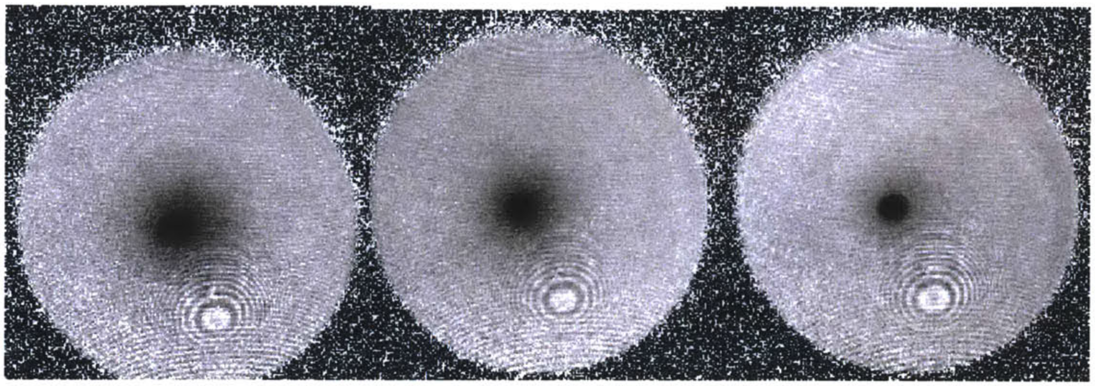

Figure 5-8: A few pictures of a the sodium BEC created under the microscope via evaporation.

## 5.4 Lattice Depth Calibration

To calibrate our lattice depth, we use the standard technique of calibration via the Kapitza-Dirac effect. This is essentially diffraction: just as light incident on a periodic structure (diffraction grating) splits into multiple orders, so does the wavefunction of electrons or atoms which feel the periodic potential of an optical lattice. To understand this phenomenon a bit more quantitatively and to see how it is used for lattice depth measurement, we imagine a condensate of atoms[2] initially in a zero-momentum state (of course, the atoms are not really in a plane wave, but such an assumption simplifies the math greatly):

$$|\Psi(t=0)\rangle = |0\rangle \tag{5.3}$$

---

[2] Or just a single atom, really; the Kapitza-Dirac effect is single-particle physics.

If we then switch on a lattice for a short time, the atoms will evolve according to the Hamiltonian

$$H = \frac{\hat{p}^2}{2m} + \frac{V_0}{2} \sin k\hat{x} \tag{5.4}$$

So after a time $t$, the atoms will be in a state

$$|\Psi(t)\rangle = e^{iV_0 t/2\hbar \sin k\hat{x} + \hat{p}^2/2m} |0\rangle \tag{5.5}$$

The Kapitza-Dirac regime is defined by switching on the lattice for times which are short compared to the time associated with the recoil energy. For sodium, this time is about 130 $\mu$ s, while for potassium, it is about 220 $\mu$ s. In this regime, the atoms do not move, so we can neglect the momentum term in the Hamiltonian. Thus

$$|\Psi(t)\rangle = e^{iV_0 t/2\hbar \sin k\hat{x}} |0\rangle , \tag{5.6}$$

which can be transformed, using a Bessel function identity, into

$$|\Psi(t)\rangle = \sum_{n=-\infty}^{\infty} J_n\left(\frac{V_0 t}{2\hbar}\right) e^{ink\hat{x}} |0\rangle , \tag{5.7}$$

or,

$$|\Psi(t)\rangle = \sum_{n=-\infty}^{\infty} J_n\left(\frac{V_0 t}{2\hbar}\right) |n\hbar k\rangle , \tag{5.8}$$

Thus, the application of a short lattice burst has the effect of splitting the condensate into discrete momentum states. The occupation of the $n^{th}$ momentum state is given by

$$P(p = n\hbar k) = J_n\left(\frac{V_0 t}{2\hbar}\right)^2 \tag{5.9}$$

Thus, by measuring the occupation of the momentum states for a variety of pulse times and lattice depths, and fitting the resulting occupations to a Bessel function, the lattice depth can be determined. In particular, the zero-momentum occupation vanishes at a time $t_0$ such that $V_0 t_0 = 4.8096\hbar$. With this method, it is not necessary to know anything about the beam waist or position; the momentum occupation gives all the information. In fact, Kapitza-Dirac can be used to align and focus a lattice properly by maximizing calculated lattice depth.

To perform Kapitza-Dirac calibration in our experiment, we create a sodium BEC in the hybrid trap under the microscope, using for the optical confinement whichever lattice we are not currently calibrating. At the end of the evaporation, we pulse on the other lattice for 4 $\mu$s, well in the Kaptiza-Dirac regime. Rather than varying the pulse time, we vary the lattice depth to avoid leaving the Kapitza-Dirac regime. An example of the resulting pictures is shown in figure 5-9. We find that the lattice depths for sodium are 1.1 mK in the y-direction and 700 $\mu$K in the x-direction. These numbers are a little lower than expected; we are currently trying to figure out why. However, even with these values, it should be possible to pin the atoms during imaging and thus take single-site resolved images.

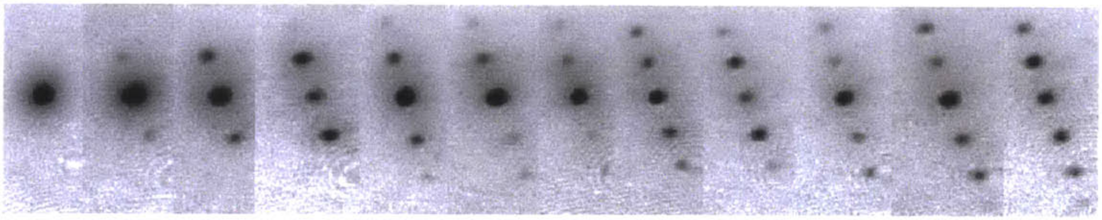

Figure 5-9: Kapitza-Dirac calibration of our optical lattice.

# Chapter 6

# Outlook

In the work described by this thesis, significant progress towards a quantum gas microscope for fermionic atoms has been achieved: magneto-optical traps for both $^{40}$K and $^{23}$Na have been realized; RF-forced evaporation in a plugged quadrupole trap has led to degenerate gases of both atomic species; via magnetic transport, these gases have been moved into position for high-resolution imaging; optics for high-resolution imaging have been set up; an optical lattice has been set up and calibrated; and optics for fluoresence imaging of $^{23}$Na via sub-Doppler cooling have been assembled.

There is still significant work to be done before the experiment is completed, i.e., before it begins to produce results. First, while a condensate of sodium atoms exists in an optical lattice, it has yet to be imaged with single-site resolution. This will require a working optical molasses for the sodium atoms, which has yet to be achieved. At the time of this writing, all of the optics for the sodium molasses are in place; in principle, all that remains for sub-Doppler cooling to be achieved is an optimization of the beam intensities and frequencies. Also, achieving single-site imaging might require slicing, or getting rid of atoms trapped in layers other than the one 10 microns from the substrate. In principle, this should be possible with RF-induced spin flips in a hybrid trap.

A second hurdle which might have to be overcome is the placement of the microscope objective with respect to the hemisphere. This placement, described in chapter 4 of this thesis, was carried out in December 2012, eight months prior to the optical lattice setup. While we hope the objective has not moved since that time, no measurements (i.e., interferometry) have been carried out to determine whether this is actually the case. Objective movement is quite possible given that it is only held in place by glue. However, with our setup, it is easy to realign the objective: the plus-sign mount can simply be removed and the objective supports can be remade.

Once both of the above challenges are solved, it will still represent the imaging of a bosonic species in an optical lattice with single-site resolution, a feat which had already been accomplished when construction on our experiment began. The final step for the present apparatus will thus be imaging of fermionic potassium atoms. However, this should not be too hard. After sodium atoms are successfully imaged, the imaging system will have been shown to work properly, leaving only cooling and molasses to be implemented for potassium. As we have already seen in this thesis, sodium and potassium are remarkably well suited for sympathetic cooling; thus the only real challenge is implementing a molasses for potassium. Once this is completed, the apparatus described in this work will be ready to probe the rich and interesting physics accessible with ultracold fermions in an optical lattice.

# Bibliography

[1] M. Atala, M. Aidelsburger, J. Barreiro, D. Abanin, T. Kitagawa, E. Demler, and I. Bloch. Direct measurement of the zak phase in topological bloch bands. *arXiv:1212.0572 [cond-mat.quant-gas]*, 2012.

[2] W. S. Bakr, A. Peng, M. E. Tai, R. Ma, J. Simon, J. I. Gillen, S. Flling, L. Pollet, and M. Greiner. Probing the superfluidtomott insulator transition at the single-atom level. *Science*, 329(5991):547–550, 2010.

[3] Waseem Bakr, Jonathon Gillen, Amy Peng, Simon Folling, and Markus Greiner. A quantum gas microscope for detecting single atoms in a hubbard-regime optical lattice. *Nature*, 462:74–77, Jul 2009.

[4] Waseem Bakr, Jonathon Gillen, Amy Peng, Simon Folling, and Markus Greiner. A mott insulator of fermionic atoms in an optical lattice. *Nature*, 471:319–324, Mar 2011.

[5] Waseem Bakr, Philipp Preiss, Eric Tai, Ruichau Ma, Jonathon Simon, and Markus Greiner. Orbital excitation blockade and algorithmic cooling in quantum gases. *Nature*, 480:500–503, Dec 2011.

[6] J. K. Chin, D.E. Miller, Y. Liu, C. Stan, W. Setiawan, C. Sanner, K. Xu, and W. Ketterle. Evidence for superfluidity of ultracold fermions in an optical lattice. *Nature*, 443:961–964, Oct 2006.

[7] K. B. Davis, M. O. Mewes, M. R. Andrews, N. J. van Druten, D. S. Durfee, D. M. Kurn, and W. Ketterle. Bose-einstein condensation in a gas of sodium atoms. *Phys. Rev. Lett.*, 75:3969–3973, Nov 1995.

[8] B. DeMarco and D. S. Jin. Onset of fermi degeneracy in a trapped atomic gas. *Science*, 285(5434):1703–1706, 1999.

[9] T. Esslinger. Fermihubbard physics with atoms in an optical lattice, 2010.

[10] Thomas Gersdorf. A quantum gas microscope for fermionic atoms. Diploma thesis, Massachusetts Institute of Technology, Physics Department, 2012.

[11] Markus Greiner, Olaf Mandel, Tilman Esslinger, Theodor W. Hansch, and Immanuel Bloch. Quantum phase transition from a superfluid to a mott insulator in a gas of ultracold atoms. *Nature*, 415:39–44, Nov 2001.

[12] R. Grimm, M. Weidemuller, and Yu. B. Ovchinnikov. Optical dipole traps for neutral atoms. *Advances in Atomic, Molecular and Optical Physics*, 2000.

[13] Hermann A. Haus. *Waves and Fields in Optoelectronics (Prentice-Hall series in solid state physical electronics).* Prentice Hall, 1984.

[14] Robert Jordens, Niels Strohmaier, Kenneth Gunter, Henning Moritz, and Tilman Esslinger. A mott insulator of fermionic atoms in an optical lattice. *Nature*, 455:204–207, Sep 2008.

[15] W. Ketterle, D.S. Durfee, and D.M. Stamper-Kurn. Making, probing and understanding Bose-Einstein condensates. In M. Inguscio, S. Stringari, and C.E. Wieman, editors, *Bose-Einstein condensation in atomic gases, Proceedings of the International School of Physics Enrico Fermi, Course CXL, Varenna, 7-17 July 1998*, pages 67–176. IOS Press, Amsterdam, 1999.

[16] W. Ketterle and N. J. van Druten. *Evaporative cooling of trapped atoms*, volume 37 of *Advances in Atomic, Molecular, and Optical Physics*, pages 181–236. Academic Press, San Diego, 1996.

[17] W. Ketterle and M.W. Zwierlein. Making, probing and understanding ultracold Fermi gases. In M. Inguscio, W. Ketterle, and C. Salomon, editors, *Ultracold Fermi Gases, Proceedings of the International School of Physics "Enrico Fermi", Course CLXIV, Varenna, 20 - 30 June 2006.* IOS Press, Amsterdam., 2008.

[18] Wolfgang Ketterle, Kendall B. Davis, Michael A. Joffe, Alex Martin, and David E. Pritchard. High densities of cold atoms in a *dark* spontaneous-force optical trap. *Phys. Rev. Lett.*, 70:2253–2256, Apr 1993.

[19] Michael Köhl, Henning Moritz, Thilo Stöferle, Kenneth Günter, and Tilman Esslinger. Fermionic atoms in a three dimensional optical lattice: Observing fermi surfaces, dynamics, and interactions. *Phys. Rev. Lett.*, 94:080403, Mar 2005.

[20] K Merloti, R Dubessy, L Longchambon, A Perrin, P-E Pottie, V Lorent, and H Perrin. A two-dimensional quantum gas in a magnetic trap. *New Journal of Physics*, 15(3):033007, 2013.

[21] Harold J. Metcalf and Peter van der Straten. *Laser Cooling and Trapping.* Springer-Verlag, New York, 1999.

[22] Alan L. Migdall, John V. Prodan, William D. Phillips, Thomas H. Bergeman, and Harold J. Metcalf. First observation of magnetically trapped neutral atoms. *Phys. Rev. Lett.*, 54:2596–2599, Jun 1985.

[23] S. Mukamel. *Principles of Nonlinear Optical Spectroscopy.* Oxford U. Press, 1995.

[24] Jee Woo Park, Cheng-Hsun Wu, Ibon Santiago, Tobias G. Tiecke, Sebastian Will, Peyman Ahmadi, and Martin W. Zwierlein. Quantum degenerate bose-fermi mixture of chemically different atomic species with widely tunable interactions. *Phys. Rev. A*, 85:051602, May 2012.

[25] Amy Peng. *Quantum Gas Microscope with Optical Lattice.* PhD dissertation, Harvard University, Physics Department, 2010.

[26] David E. Pritchard. Cooling neutral atoms in a magnetic trap for precision spectroscopy. *Phys. Rev. Lett.*, 51:1336–1339, Oct 1983.

[27] E. L. Raab, M. Prentiss, Alex Cable, Steven Chu, and D. E. Pritchard. Trapping of neutral sodium atoms with radiation pressure. *Phys. Rev. Lett.*, 59:2631–2634, Dec 1987.

[28] Vinay Ramasesh. Towards a quantum gas microscope for fermionic atoms. Senior thesis, Massachusetts Institute of Technology, Physics Department, 2012.

[29] Jun John Sakurai. *Modern Quantum Mechanics.* Addison-Wesley Publishing Company, Reading, MA, Revised edition, 1994.

[30] Bahaa E. A. Saleh and Malvin C. Teich. *Fundamentals of Photonics (Wiley Series in Pure and Applied Optics).* John Wiley & Sons, 1st edition, August 1991.

[31] Daniel Steck. *Quantum Chaos, Transport, and Decoherence in Atom Optics.* PhD dissertation, UT Austin, Physics Department, 2001.

[32] Tobias Gerard Tiecke. *Feshbach resonances in ultracold mixtures of the fermionic quantum gases 6Li and 40K.* PhD dissertation, University of Amsterdam, Physics Department, 2009.

[33] Christoph Weitenberg. *Single-Atom Resolved Imaging and Manipulation in an Atomic Mott Insulator.* PhD dissertation, LMU Munchen, Physics Department, 2011.

[34] Sebastian Will. *Interacting bosons and fermions in three-dimensional optical lattice potentials: from atom optics to quantum simulation.* PhD dissertation, University of Mainz, Physics Department, 2011.

# Appendix A

# Lattice Depth Calculation

This appendix derives the numerical constant of proportionality between lattice beam power and lattice depth (in both recoil energies and temperature) for sodium and potassium in our optical lattice. Start with the intensity of a Gaussian beam at its focus, with waists[1] $w_x$ and $w_y$, which varies as

$$I(x,y) = I_0 e^{-2(x^2/w_x^2+y^2/w_y^2)} \tag{A.1}$$

We integrate to get an expression for power, P:

$$\begin{aligned} P &= I_0 \int e^{-2x^2/w_x^2} dx \int e^{-2y^2/w_y^2} dy && \text{(A.2)} \\ &= I_0 \frac{\pi w_x w_y}{2} && \text{(A.3)} \end{aligned}$$

Interestingly, the power is the intensity times one half of the area of an ellipse formed by $w_x$ and $w_y$ as semiaxes.

Now we use the formula for dipole potential derived in the main text:

$$U_{dip}(\vec{r}) = \frac{3\pi c^2}{2w_0^3} \left( \frac{\Gamma}{\omega_0 - \omega} + \frac{\Gamma}{\omega_0 + \omega} \right) I(\vec{r}) \tag{A.4}$$

With a 1064 lattice like the one in our experiment, the detuning is large enough that one shouldn't use the rotating wave approximation to get rid of the $\omega_0 + \omega$ term: in the case of potassium, for example, $\omega_0$ is about $2.5 \times 10^{15} Hz$, while for 1064 nm, $\omega$ is $1.8 \times 10^{15} Hz$. Ignoring the smaller denominator would thus lead to an error fo about 15%.

---

[1] Our waists are roughly 35 and 100 microns

Table A lists the parameters needed to calculate the lattice depths for sodium and potassium. Since each has both a D1 and D2 transition, we must slightly modify the formula above for dipole potential, which was derived assuming a perfect two-level system. For linearly polarized light, this modification simply takes the form [12]:

$$U_{dip}(\vec{r}) = \sum_{i=D1,D2} c_i \frac{\pi c^2}{2w_{i0}^3} \left( \frac{\Gamma_i}{\omega_{i0} - \omega} + \frac{\Gamma_i}{\omega_{i0} + \omega} \right) I(\vec{r}) \tag{A.5}$$

where $c_i$ is 2 for the D2 transition and 1 for D1. Using the equation above, we get

Table A.1: Parameters for calculating dipole potentials

| Element | Parameter | Value (Hz) |
|---|---|---|
| Potassium-40 [32] | D1 $\Gamma/2\pi$ | $5.956 \times 10^6$ |
| | D2 $\Gamma/2\pi$ | $6.035 \times 10^6$ |
| | D1 $\nu = \omega_0/2\pi$ | $3.893 \times 10^{14}$ |
| | D2 $\nu = \omega_0/2\pi$ | $3.910 \times 10^{14}$ |
| Sodium-23 [31] | D1 $\Gamma/2\pi$ | $9.765 \times 10^6$ |
| | D2 $\Gamma/2\pi$ | $9.795 \times 10^6$ |
| | D1 $\nu = \omega_0/2\pi$ | $5.083 \times 10^{14}$ |
| | D2 $\nu = \omega_0/2\pi$ | $5.088 \times 10^{14}$ |

the following:

$$U_{Na}(\vec{r}) = 7.2038 \times 10^{-37} m^2 s I(\vec{r}) \tag{A.6}$$

$$U_K(\vec{r}) = 1.8432 \times 10^{-36} m^2 s I(\vec{r}) \tag{A.7}$$

For the peak depth we replace $I(\vec{r})$ with $I_0$ and use the relationship between intensity and power:

$$U_{Na,0} = 1.3104 \times 10^{-28} s \times P \tag{A.8}$$

$$U_{K,0} = 3.353 \times 10^{-28} s \times P \tag{A.9}$$

Expressing in more natural units of $\mu K$ per Watt:

$$U_{Na,0} = 9.491\mu K \times P/Watt \tag{A.10}$$

$$U_{K,0} = 24.29\mu K \times P/Watt \tag{A.11}$$

Were we using a dipole trap, this would be the correct depth. However, because we use a lattice configuration, we gain a factor of four in intensity compared to power:

$$U_{Na,0} = 37.964\mu K \times P/Watt \tag{A.12}$$

$$U_{K,0} = 97.16\mu K \times P/Watt \tag{A.13}$$

Another way of expressing lattice depth is to compare it to the recoil energy,[2] $E_R = h^2/2m\lambda^2$. For sodium in a 1064 nm lattice, $E_R$ is 0.368 $\mu K$, while for potassium it is 0.216 $\mu K$. This gives us

$$U_{Na,0} = 103.2E_R^{Na} \times P/Watt \tag{A.14}$$

$$U_{K,0} = 449.8E_R^{K} \times P/Watt \tag{A.15}$$

These last two equation sets are the ones we wanted. Note that since these quantities scale inversely with beam area, these numbers can easily be scaled for beams of a different geometry.

---

[2] It seems natural that the $\lambda$ in the recoil expression should be the actual lattice separation, not the wavelength of the light. But convention has it the other way, so in the calculations above we use $\lambda = 1064$ nm.

# Appendix B

# MATLAB Code for Calculating Atom Numbers and Phase Space Densities

This appendix presents code we used during our evaporation of sodium and potassium to calculate the phase space density and atom number in a cloud. It searches a given directory for new absorption images, then converts the image file into an array of optical density values. Fitting these to a Gaussian, it then extracts the relevant parameters from the image.

```
function GUI_PSDAtomNumber
% GUI_PSDAtomNumber Plots the phase-space density and atom number of a
% cloud from an absorption image

   %  Create and then hide the GUI as it is being constructed.
   f = figure('Visible','off','Position',[360,500,940,1000]);

   % Set Region of interest values (crop the absorption image)
   xmin=1;
   ymin=50;
   xmax=512;
   ymax=512;

   % Set Parameter Values
   sigma0=8e-14;%*(767/589)^2 if we want Potassium
   pixelsize=16e-6*(29/30);
```

```
kb=1.38e-23;
tof=6e-3;
mass=23*1.67e-27;
muB=9.27e-24;
mF=2;
VGrad=3.6;
Baxgrad=mF*4.2*VGrad/4.5;
planck=6.63e-34;

%set a save counter
savecount=0;

%debugging: set an update counter
updatecount=0;
foundcount=0;
newsavename = '';


offset_x=400;
offset_y=720;
%  Construct the components.
ht_roi = uicontrol('Style','text','String','Region of Interest',...
        'Position',[300+offset_x,245+offset_y,100,15]);
h_xmin = uicontrol('Style','edit','String',num2str(xmin),...
        'Position',[315+offset_x,225+offset_y,30,18],...
        'Callback',{@XMin_Callback});
h_ymin = uicontrol('Style','edit','String',num2str(ymin),...
        'Position',[315+offset_x,200+offset_y,30,18],...
        'Callback',{@YMin_Callback});
h_xmax = uicontrol('Style','edit','String',num2str(xmax),...
        'Position',[385+offset_x,225+offset_y,30,18],...
        'Callback',{@XMax_Callback});
h_ymax = uicontrol('Style','edit','String',num2str(ymax),...
        'Position',[385+offset_x,200+offset_y,30,18],...
        'Callback',{@YMax_Callback});
ht_xmin = uicontrol('Style','text','String','xmin',...
        'Position',[280+offset_x,225+offset_y,25,15]);
ht_ymin = uicontrol('Style','text','String','ymin',...
        'Position',[280+offset_x,200+offset_y,25,15]);
ht_xmax = uicontrol('Style','text','String','xmax',...
        'Position',[350+offset_x,225+offset_y,32,15]);
ht_ymax = uicontrol('Style','text','String','ymax',...
        'Position',[350+offset_x,200+offset_y,32,15]);
ht_params = uicontrol('Style','text','String','Parameters',...
        'Position',[315+offset_x,170+offset_y,60,15]);
h_mF = uicontrol('Style','edit','String',num2str(mF),...
        'Position',[360+offset_x,145+offset_y,30,18],...
```

```
           'Callback',{@mF_Callback});
    h_grad = uicontrol('Style','edit','String',num2str(VGrad),...
           'Position',[360+offset_x,125+offset_y,30,18],...
           'Callback',{@grad_Callback});
    h_tof = uicontrol('Style','edit','String',num2str(tof*10^3),...
           'Position',[360+offset_x,105+offset_y,30,18],...
           'Callback',{@tof_Callback});
    ht_mF = uicontrol('Style','text','String','mF',...
           'Position',[300+offset_x,148+offset_y,25,15]);
    ht_grad = uicontrol('Style','text','String','Grad',...
           'Position',[300+offset_x,128+offset_y,25,15]);
    ht_tof = uicontrol('Style','text','String','ToF (ms)',...
           'Position',[300+offset_x,108+offset_y,50,15]);
    h_resetNoSave=uicontrol('Style','pushbutton','String',...
        'Reset Data WithOUT Saving','Position',...
        [275+offset_x,70+offset_y,150,25],'Callback',...
        {@reset_Callback});
    h_resetYesSave=uicontrol('Style','pushbutton','String',...
        'Reset Data With Saving','Position',...
        [275+offset_x,40+offset_y,150,25],'Callback',...
        {@save_Callback});
    h_saveName=uicontrol('Style','edit','String','Enter Filename',...
        'Position',[275+offset_x,10+offset_y,150,25],...
        'Callback',{@saveName_Callback});


    % Create the data to plot.
    AtomHistory_data = [];
    PSDHistory_data = [];

    % Set Region of Interest
    roi = [xmin xmax ymin ymax];



    % Initialize the GUI.
    % Change units to normalized so components resize
    % automatically.
    set([f,h_xmin,h_ymin,h_xmax,h_ymax,ht_xmin,ht_xmax,ht_ymin,...
        ht_ymax,ht_roi,ht_params,h_mF,h_grad,h_tof,ht_mF,ht_grad,...
        ht_tof,h_resetNoSave,h_resetYesSave],...
     'Units','normalized');
    % Assign the GUI a name to appear in the window title.
    set(f,'Name','PSD AtomNumber Analyzer')
    % Move the GUI to the center of the screen.
    movegui(f,'east')
    % Make the GUI visible.
```

```
 set(f,'Visible','on');
 %Create a plot in the axes.
 subplot(4,1,1);
 title('Most Recent Image');
 subplot(4,1,2);
 scatter(1:length(PSDHistory_data), log10(PSDHistory_data));
 title('Log PSD History');
 subplot(4,1,3);
 scatter(1:length(AtomHistory_data), log10(AtomHistory_data));
 title('Log Atom Number History');
 subplot(4,1,4);
 scatter(log10(AtomHistory_data),log10(PSDHistory_data));
 title('Log-Log Atom Number vs. PSD');
 xlabel('Log Atom Number');
 ylabel('Log PSD');


timerObject = timer('TimerFcn',{@NewFit},'ExecutionMode',...
    'fixedSpacing','Period',1.0);

 start(timerObject);

 %  Callbacks for GUI_PSDAtomNumber.

  function saveName_Callback(source,eventdata)
      %Called when user types in the savename window
      %set the savename
      newsavename=get(source,'String');
  end

 function XMin_Callback(source,eventdata)
 % Called when user types in the xmin window
 % Set the xmin value
       xmin=str2num(get(source,'String'));
          roi = [xmin xmax ymin ymax];
 end

  function XMax_Callback(source,eventdata)
 % Called when user types in the xmax window
 % Set the xmax value
       xmax=str2num(get(source,'String'));
          roi = [xmin xmax ymin ymax];
  end

  function YMin_Callback(source,eventdata)
  % Called when user types in the ymin window
  % Set the ymin value
```

```
         ymin=str2num(get(source,'String'));
            roi = [xmin xmax ymin ymax];
    end

    function YMax_Callback(source,eventdata)
    % Called when user types in the ymax window
    % Set the ymax value
        ymax=str2num(get(source,'String'));
           roi = [xmin xmax ymin ymax];
    end

    function mF_Callback(source,eventdata)
        %Called when user types in the mF window
        %Note that we have to evaluate Baxgrad again
        mF=str2num(get(source,'String'));
        Baxgrad=mF*4.2*VGrad/4.5;;
    end

    function grad_Callback(source,eventdata)
        %Called when user types in the mF window
        %Note that we have to evaluate Baxgrad again
        VGrad=str2num(get(source,'String'));
        Baxgrad=mF*4.2*VGrad/4.5;;
    end

    function tof_Callback(source,eventdata)
        %Called when user types in the mF window
        %Note that we have to evaluate Baxgrad again
        tof=str2num(get(source,'String'))/10^3;
    end

    function reset_Callback(source,eventdata)
        %Called when user presses the 'Reset' button
        %Sets all the history variables back to empty arrays
         AtomHistory_data = [];
         PSDHistory_data = [];

        %PLOT 2: Plots the PSD History
        subplot(4,1,2);
        scatter(1:length(PSDHistory_data), log10(PSDHistory_data));
        title('Log PSD History');

        %PLOT 3: Plots the Atom Number History
        subplot(4,1,3);
        scatter(1:length(AtomHistory_data), log10(AtomHistory_data));
        title('Log Atom Number History');

        %PLOT 4: Plots Log of atom number versus log of PSD
        subplot(4,1,4);
        scatter(log10(AtomHistory_data),log10(PSDHistory_data));
        title('Log-Log Atom Number vs. PSD');
        xlabel('Log Atom Number');
        ylabel('Log PSD');
    end

    function save_Callback(source,eventdata)
        %Called when user presses the 'Reset' button
        %Saves the history variables, and then
        %Sets all the history variables back to empty arrays
        c=clock;
        timestring=strcat(num2str(c(4)),...
            num2str(c(5),'%02.0f'),num2str(c(6),'%02.0f'));

        if strcmpi(newsavename,'Enter Filename')
            newsavename='';
        end

        save(strcat(newsavename,timestring,...
            'AtomNumber.mat'),'AtomHistory_data');
        save(strcat(newsavename,timestring,...
            'PSD.mat'),'PSDHistory_data');

         AtomHistory_data = [];
         PSDHistory_data = [];

        %PLOT 2: Plots the PSD History
        subplot(4,1,2);
        scatter(1:length(PSDHistory_data),...
            log10(PSDHistory_data));
        title('Log PSD History');

        %PLOT 3: Plots the Atom Number History
        subplot(4,1,3);
        scatter(1:length(AtomHistory_data),...
            log10(AtomHistory_data));
        title('Log Atom Number History');

        %PLOT 4: Plots Log of atom number versus log of PSD
        subplot(4,1,4);
        scatter(log10(AtomHistory_data),...
            log10(PSDHistory_data));
        title('Log-Log Atom Number vs. PSD');
        xlabel('Log Atom Number');
        ylabel('Log PSD');
    end

    function NewFit(source,eventdata)
         updatecount=updatecount+1;
         %Find all the new fit files in the directory
         newFits=dir('*.fits');
         %If there are some more fits to be done...
         if(not(isempty(newFits)))
           foundcount=foundcount+1;
           %Read the image file
           datfile=fitsread(newFits(1).name);
           img=datfile(:,:,4);
           %crop the image file
           img=img(roi(3):roi(4),roi(1):roi(2));
           %remove infinities, NaNs, and zeros
           img(isinf(img))=0;
           img(isnan(img))=0;
           img(img<.005)=0.005;
           img=-log(img);
           %Move the image file to a 'done' folder
           movefile(newFits(1).name,'done');


           %Fit image with a Gaussian and
           %extract atom number, temperature,
           %PSD, and collision rate
           [cx,cy,sx,sy,PeakOD,bg] = Gaussian2D(img);
           AtomNumber_data=round(2*pi*sx*sy*PeakOD*...
               pixelsize^2/sigma0);
           Temperature_data=round(((sx+sy)/2*...
               pixelsize/tof)^2*mass/kb*1e9);
           PSD_data= (((0.5*muB*Baxgrad)^3)*...
               ((planck^2/(2*pi*mass))^(3/2))*...
               AtomNumber_data/((kb*Temperature_data*1e-9)...
               ^(9/2)))/32;
           ColRate_data=PSD_data^(2.5/4.5)*...
               (AtomNumber_data/1e3)^(2/4.5);

           %PLOT 1: Plots the image and displays the parameters
           subplot(4,1,1);
           imagesc(img,[0,1.3]);
           axis([xmin xmax ymin ymax]);
           axis equal;
           title(strcat('Image ', num2str(foundcount),': ',..
           'AtomNumber=',num2str(AtomNumber_data),' ',...
           'T=',num2str(Temperature_data),'nK,    ', 'PSD=',...
           num2str(log10(PSD_data)),' ,colrate=',...
           num2str(ColRate_data)));

           %Updates the history variables
           AtomHistory_data=[AtomHistory_data AtomNumber_data];
           PSDHistory_data = [PSDHistory_data PSD_data];

           %PLOT 2: Plots the PSD History
           subplot(4,1,2);
           scatter(1:length(PSDHistory_data),...
               log10(PSDHistory_data));
           title('Log PSD History');

           %PLOT 3: Plots the Atom Number History
           subplot(4,1,3);
           scatter(1:length(AtomHistory_data),...
               log10(AtomHistory_data));
           title(strcat('Log Atom Number History:  LogAtomNumber='...
               ,num2str(log10(AtomHistory_data...
               (length(AtomHistory_data))))));

           % PLOT 4: Plots Log of atom number versus log of PSD
           subplot(4,1,4);
           scatter(log10(AtomHistory_data),log10(PSDHistory_data));
                   title('Log-Log Atom Number vs. PSD');
           xlabel('Log Atom Number');
           ylabel('Log PSD');
           hleg1=legend('Fermi2','Fermi1','3.6','2.4');
         end
    end


end
```